Subsurface structure of the Solfatara volcano (Campi Flegrei caldera, Italy) as deduced from joint seismic-noise array, volcanological and morphostructural analysis.

Simona Petrosino, corresponding author
Istituto Nazionale di Geofisica e Vulcanologia, Sezione di Napoli - Osservatorio Vesuviano,
Via Diocleziano, 328 – Naples, Italy
simona.petrosino@ov.ingv.it

Norma Damiano
Università degli Studi di Napoli Federico II, Italy
damiano@ov.ingv.it

Paola Cusano
Istituto Nazionale di Geofisica e Vulcanologia, Sezione di Napoli - Osservatorio Vesuviano, Italy
Via Diocleziano, 328 – Naples, Italy
paola.cusano@ov.ingv.it

Mauro Antonio Di Vito
Istituto Nazionale di Geofisica e Vulcanologia, Sezione di Napoli - Osservatorio Vesuviano, Italy
Via Diocleziano, 328 – Naples, Italy
mauro.divito@ov.ingv.it

Sandro de Vita
Istituto Nazionale di Geofisica e Vulcanologia, Sezione di Napoli - Osservatorio Vesuviano, Italy
Via Diocleziano, 328 – Naples, Italy
sandro.devita@ov.ingv.it

Edoardo Del Pezzo
Istituto Nazionale di Geofisica e Vulcanologia, Sezione di Napoli - Osservatorio Vesuviano, Italy
Via Diocleziano, 328 – Naples, Italy
Instituto Andaluz de Geofisica, Universidad de Granada, Spain
edoardo.delpezzo@ov.ingv.it

Abstract

The joint application of different seismological techniques for seismic noise analysis, and the results of a volcanological and morphostructural survey, have allowed us to obtain a detailed and well constrained image of the shallow crustal structure of the Solfatara volcano (Campi Flegrei caldera, Italy). Horizontal-to-vertical spectral ratios, inversion of surface wave dispersion curves and polarization analysis provided resonance frequencies and peak amplitudes, shear-wave velocity profiles and polarization pattern of coherent ambient noise. These results, combined in a unique framework, indicate that the volcanic edifice is characterized by lateral and vertical discontinuities and heterogeneities in terms of shear-wave velocity, lithological contrasts and structural setting. The interpretation of the seismological results, with the volcanological and morphostructural constraints, supports the hypothesis that the volcano has been characterized by a complex and intense activity, with the alternation of constructive and destructive phases, during which magmatic and phreatomagmatic explosions built a complex tuff-cone, later reworked by atmospheric agents and altered by hydrothermal activity. The differences in the velocity structure between the central and eastern parts of the crater have been interpreted as resulting from a possible eastward migration of the eruptive vent along the deformational features affecting the area, and to the presence of viscous lava and lithified tuff bodies within the feeding conduits, which are buried under a covering of reworked materials of variable thickness. The observed fault and fracture systems, partially inherited from regional structural setting and exhumed during volcanism and ground deformation episodes also seems to strongly control wave propagation, affecting the noise polarization properties.

1. Introduction

Seismic noise represents an attractive tool to investigate the shallow crustal properties due to the speed and ease of data acquisition and the relative simplicity of analysis. Much information can be extracted

by applying both single- and multi-channel techniques to microtremor. Single-station methods, such as Horizontal-to-Vertical (H/V) spectral ratio [*Nakamura*, 1989], have been extensively employed in seismic hazard studies to determine the fundamental resonance frequency and the amplification of a given site [*Alfaro et al.*, 2001; *Parolai et al.*, 2004; *Maresca et al.*, 2006]. Although there is still a debate about the correct interpretation of the H/V ratio, especially regarding the correlation between the peak amplitude and the actual site amplification [*Luzon et al.*, 2001; *Malischewsky and Scherbaum*, 2004], many efforts have recently been made to prove the effectiveness of the method through numerical simulations [*Bonnefoy-Claudette et al.*, 2006]. Moreover, standard criteria for a correct noise acquisition and rules for the assessment of the reliability of the results have been defined (SESAME European Project, Deliverable D23.12, available from http://sesame-fp5.obs.ujf-grenoble.fr).

When multiple seismometers are available, array techniques can be used to determine the surface wave dispersion curves and the 1-D path integrated shear-wave (S) velocity profile from their inversion. Even in the presence of a complicated medium, 1-D dispersion carries information about the average properties of the earth's crust and its inversion is a good approximation of the velocity structure [*Dziewonski and Hales*, 1972; *Ekström et al.*, 1997; *Ritzwoller and Levshin*, 1998]. In addition, detailed 2-D and 3-D images of the crust can be obtained combining several 1-D velocity profiles [*Picozzi et al.*, 2009; *Stehly et al.*, 2009].

Frequency-Wavenumber (f-k) [*Lacoss et al.*, 1969] and Spatial Autocorrelation (SPAC) [*Aki*, 1957, 1965] techniques have become very popular for the analysis of ambient vibrations. The initial limits of the SPAC method related to the circular geometry have been overcome by adapting the method to non-circular configurations [*Bettig et al.*, 2001]. All these techniques have been successfully applied, demonstrating that the inversion of dispersion curves from microtremor data can provide fine resolution of the shallow S-wave velocity model [*Bozdag and Kocauglu*, 2005; *Di Giulio et al.*, 2006; *Maresca et al.*, 2006]. Subsurface structure down to a scalelength of the order of 500 m has been

retrieved for several volcanoes, such as Masaya [*Métaxian et al.*, 1997], Stromboli [*Chouet et al.*, 1998, *Petrosino et al.*, 1999, 2002], Vesuvius [*Saccorotti et al.*, 2001], Kilauea [*Saccorotti et al.*, 2003] and Arenal [*Mora et al.*, 2006]. High-resolution seismic images of the shallow crust are extremely important in volcanic areas, because the heterogeneous subsurface structure represents a complex propagation medium for seismic waves and clearly influences the wavefield. Some authors have shown that unconsolidated, alternating layers of ash, pumice and lithified rocks generates stronger scattering than in ordinary crust [*Wegler and Luhr*, 2001; *Wegler*, 2003; *Parsiegla and Wegler*, 2008]. Moreover, recent studies based on numerical simulations have demonstrated how different shallow crustal models significantly change the shape of the seismograms of volcanic earthquakes, thus affecting the accuracy of the location and the polarization pattern, and causing bias in the source inversion [*Cesca et al.*, 2008; *Bean et al.*, 2009; *Lokmer and Bean*, 2010]. Therefore accurate knowledge of the velocity structure is crucial for a correct separation of the observed signal into source and path/site effects, improving the definitions of the mechanisms that trigger and govern volcanic activity.

An intriguing observation has been recently made by *Rigano et al.* [2008], who demonstrated that further information about the medium structure is provided by microtremor. These authors, focusing on ambient noise polarization at Mt. Etna, found that its direction was somewhat controlled by the presence of faults, and it was never parallel to the fault strike. Although an influence of faults on the polarization of earthquake ground motion has been found by many authors and been explained in term of a waveguide mechanism [*Li et al.*, 1994; *Rovelli et al.*, 2002; *Ben-Zion et al.*, 2003], the systematic tendency of seismic noise to be polarized has been observed for the first time at Mt. Etna and the mechanism responsible for this characteristic is still not clear. *Rigano et al.* [2008] suggest, as possible hypotheses to be further investigated, that the noise polarization is caused by anisotropy or by the resonance of seismic waves in the fault zone.

In this paper we combine spectral ratio, surface wave dispersion inversion and polarization techniques

105 in a unique framework with the aim of extracting a coherent and robust estimate of the fine crustal
106 structure in the first 200 meters below the Solfatara volcano. In particular, the H/V spectral ratio
107 technique has provided the resonance frequency and the peak amplitude values for 68 sampled sites;
108 the S-wave velocity profiles in 5 different areas of the crater have been retrieved from the inversion of
109 surface wave dispersion curves estimated by f-k and SPAC methods; the polarization pattern of seismic
110 noise evidences possible correlations with the orientation of the structural features of the volcano. In
111 addition we present results from a detailed volcanological and morphostructural survey aimed at
112 constraining the geophysical interpretation. The seismological techniques, together with the geological
113 information mainly derived from the volcanological and morphostructural survey, have allowed us to
114 obtain a realistic 3-D image of the shallow crustal structure in this area.
115
116 **2. Geological Framework**
117 **2.1. The Campi Flegrei Caldera**
118 The Solfatara volcano is located in the central part of the repeatedly collapsed Campi Flegrei caldera
119 (CFc), and is one of the youngest volcanoes formed within this active volcanic field [*Rosi and Sbrana*,
120 1987; *Orsi et al.*, 1996; *Isaia et al.*, 2009]. Resurgence affected the central part of the caldera, causing
121 the uplift of a number of differentially displaced blocks, the most uplifted of which is the La Starza
122 marine terrace that has been raised up about 90 m in the past 10 ka [*Di Vito et al.*, 1999]. Resurgence
123 and volcanism in the past 15 ka are strictly related; indeed intense volcanism was preceded and
124 accompanied by intense phases of ground deformation. At least 72 mainly explosive eruptions occurred
125 after the youngest caldera collapse; the last one, Monte Nuovo (1538 AD) was preceded by significant
126 ground uplift, mainly concentrated in the vent area [*Di Vito et al.*, 1987].
127 Ground uplift and subsidence events of the caldera floor, known in the geological literature as
128 bradyseism [*Orsi et al.*, 1999 and references therein], occurred repeatedly up today, with a maximum

129 deformation area located around the town of Pozzuoli. Different approaches aimed at reconstructing the
130 processes governing the recent caldera dynamics have revealed that these unrest episodes were related
131 to a complex interaction between the deep magmatic source and the shallow hydrothermal system [*Orsi*
132 *et al.*, 1999; *Chiodini et al.*, 2001; *Battaglia et al.*, 2006; *Zollo et al.*, 2008; *D'Auria et al.*, 2011;
133 *Falanga and Petrosino*, 2012].
134 The deformation pattern of both caldera floor and resurgent block of different sectors of the CFc is
135 controlled by the NW-SE and NE-SW trending regional structures [*Orsi et al.*, 1996; *de Vita et al.*,
136 1999; *Di Vito et al.*, 1999] that are partially reactivated during each bradyseismic crisis [*Orsi et al.*,
137 1999]. Detailed structural analyses indicate the particular role of the NW-SE trending faults and
138 fissures in the deformation and volcanism of the Solfatara area [*Vilardo et al.*, 2010]. These structures
139 also control the seismic activity that generally accompanies the uplift phases, and which has been
140 interpreted as the response to stress field changes induced by ground deformation [*De Natale et al.*,
141 1987; *Bianco et al.*, 2004; *Saccorotti et al.*, 2007; *Cusano et al.*, 2008].
142 The regional stress field in the Solfatara area, which also controls the volcanism of the CFc, is mainly
143 due to the anticlockwise rotation of the Italian peninsula. This rotation is related to the opening of the
144 Tyrrhenian basin, which occurred through the activation of Plio-Quaternary extensional processes that
145 affected the Tyrrhenian margin of the Apennine chain. The onset of volcanism at about 0.7 Ma [*Amato*
146 *and Montone*, 1997 and references therein], reflects a recent extensional pulse, which caused the
147 activation of NW-SE trending normal faults that have downthrown south-westward this margin, and
148 NE-SW trending normal to strike slip faults, which have been interpreted as transverse structures
149 [*Liotta*, 1991; *Faccenna et al.*, 1994]. A horst-and-graben type structural pattern in the region was
150 generated in relation to this tectonism, and the Campanian plain – in which the CFc is located -
151 represents the largest of these grabens. Within this regional stress field the conditions for magma to
152 form and rise to surface were established. At a regional scale volcanism occurred along a NW-SE

153 trending belt, parallel to the margin of the chain; however the main volcanic vents are located at the
154 intersection between NW-SE and NE-SW trending fault systems, within transverse depressions, and are
155 dominated by caldera-forming eruptions [*de Vita et al.*, 2005 and references therein]. This kind of
156 stress field is characterized by a NE-SW to ENE-WSW trending σ_3 (horizontal minimum stress),
157 perpendicular to the main extensional structures, a NW-SE to NNW-SSE trending σ_2 (horizontal
158 maximum stress), perpendicular to the main transfer structures, and a vertical σ_1 [*Amato and Montone*,
159 1997].
160
161 **2.2. The Solfatara Volcano**
162 The Solfatara volcano [*Di Vito et al.*, 1999; *Isaia et al.*, 2009] is a tuff cone located at 100 m above sea
163 level, about 2 km NE of the town of Pozzuoli (Figure 1). It was formed at 3,815±55 a b.p. during the
164 third epoch of volcanic activity of the CFc [*Di Vito et al.*, 1999]. Its crater is a 0.5 x 0.6 km sub-
165 rectangular structure, the geometry of which is mainly due to the control exerted by N40-50W and
166 N50E trending fault systems. These systems crosscut the area (Figure 1) and have been active many
167 times, before and after the formation of the crater, likely reactivating pre-existing regional structures
168 during the main volcano-tectonic events that affected the CFc [*Orsi et al.*, 1996, 1999; *de Vita et al.*,
169 1999]. The morphology of the Solfatara volcano has been interpreted as formed by a multivent activity,
170 which generated a complex sequence that includes the S. Maria delle Grazie Tephra, Mt. Olibano
171 Lavas and Tephra, the Accademia Lava Dome and the Solfatara Tephra [*Isaia et al.*, 2009]. Multivent
172 activity, often characterized by vent migration along structurally-controlled fissures, is a quite common
173 feature in the CFc, as it has been reported also for other recent events [*Rosi and Sbrana*, 1987; *de Vita*
174 *et al.*, 1999; *Isaia et al.*, 2004; 2009; *Orsi et al.*, 2009; *Tonarini et al.*, 2009; *Di Vito et al.*, 2010].
175 Although soil diffuse degassing occurs throughout the entire area of the Solfatara crater [*Chiodini et*
176 *al.*, 2001], fumarolic activity is mainly concentrated in its south-eastern part (Bocca Grande and Bocca

177 Nuova area) at the intersection between the N50W and the N50E trending fractures that border the
178 north-eastern and south-eastern part of the crater, respectively, and in the north-eastern area (Stufe)
179 along the main NW-SE trending fault, cutting the crater. The hydrothermally altered zone also extends
180 outside the crater, along the prolongation of these structures, in areas in which the intersection of
181 fractures belonging to the same systems is clearly evident (Figure 1). The central part of the Solfatara
182 crater is occupied by the Fangaia mud pool, at which the water-table emerges and a continuous rising
183 of hydrothermal fluids generates diffuse bubbling. In this area a 0.7 m wide, N50E trending extensional
184 fracture, opened during the 1982-84 bradyseismic crisis [*Acocella et al.*, 1999]. Soil temperature
185 distribution [*Chiodini et al.*, 2001] also shows the direct control exerted by the structures on the heat
186 flux, as demonstrated by the alignment of the highest temperature values along the direction of the
187 main fracture systems, in the north-eastern and south-eastern parts of the crater, as well as in the
188 Fangaia area [*Granieri et al.*, 2010]. On the contrary, the north-western sector of the crater is relatively
189 inactive with respect to the heat flux and fumarolic activity.
190 Geophysical and hydrogeological investigations at the Solfatara volcano [*Bruno et al.*, 2007] provide
191 images of the shallow and intermediate subsurface of the crater. These authors, using electromagnetic
192 and electrical data, recognized two electrical zones: an outcropping resistive layer (A) overlying a
193 conductive one (B). The latter has an irregular top, crops out in the mud pool area and is up to 20-50 m
194 deep in the northeastern side of the crater. According to *Bruno et al.* [2007] layer A represents a clayey,
195 non-saturated zone, and layer B corresponds to a hydrothermal aquifer recharged through condensation
196 of geothermal fluids.
197 At a deeper level, evidence of a gas or fluid reservoir beneath the Solfatara area comes from the recent
198 seismic attenuation imaging of Campi Flegrei by *De Siena et al.* [2010] who recognize a vertically
199 extending, high attenuation structure. This result is compatible with that of *Battaglia et al.* [2008] who

observed a high V_P/V_S anomaly in the southwestern part of the Solfatara, as expected for a strongly fractured medium permeated by fluids.

3. Data Acquisition and Analysis

In the following subsections we present the results of the volcanological, structural and seismic surveys that we carried out at the Solfatara, and we propose a multidisciplinary approach in which the geological and geophysical measurements integrate to image at a high level of detail the shallow crustal structure of such a complex volcano.

3.1. Volcanological and Structural Survey

The volcanological and structural field survey of the Solfatara volcanic edifice carried out in the present work was preceded by a photo aerial analysis and interpretation. It aimed at an optimal description of the pyroclastic sequence associated with the activity of the Solfatara vent area, and at a detailed reconstruction of the crater morphology, structure and deformational history. The reconstructed sequence of the Solfatara Tephra (Table 1) includes a basal breccia, which directly lies above the Mt. Olibano lava dome, and a phreatomagmatic sequence of stratified fine- and coarse-ash surge-beds. The Solfatara Tephra also includes two surfaces of angular unconformity, which subdivide into three portions the entire sequence. The first surface (Angular Unconformity 1 –Table 1) separates the basal breccia from the overlying stratified succession, which is in turn separated into a lowermost, thicker part, and an upper, thinner portion by the second surface (Angular Unconformity 2 – Table 1).

The morphostructural survey highlighted the main morphological features of the area and the mutual relationships among the different fracture systems. The south-eastern part of the crater wall is carved into the Mt. Olibano lava dome, which was extruded slightly before the Solfatara activity, whereas its easternmost part is partially deformed by a minor, sub-rounded, rim structure nested within the main

crater (Figure 1). The area is affected by dominant NW-SE trending faults and fractures which crosscut the Solfatara area and its external parts, downthrowing to NE (i.e. toward the Agnano plain) the marine deposits of the La Starza marine terrace. Both internal and external slopes of the volcano show rectilinear parts (residual fault scarps), triangular facets and aligned drainage lines (lineation of the north-eastern outer slopes). This fault system is intersected by the NE-SW system also well evidenced by rectilinear valleys and slopes, such as the south-eastern inner slope of the Solfatara crater, and the valleys crosscutting both the Solfatara volcano and La Starza marine terrace (Figure 1). Also the fracture that opened in the crater floor during the last large bradyseismic event (1982-1984) had this same orientation. Finally the faults and fractures trending around NS and EW are well visible along the outer slopes of the volcano, whereas in the crater floor area they are likely masked by the reworked deposits filling the crater. At a smaller scale the survey suggests that the geometry of the Solfatara crater is only partially inherited from pre-existing fault and fracture systems and their morphological evolution.

Finally, a meso-structural survey has been carried out in selected sites both inside and outside the Solfatara crater, in order to highlight the mutual relationships among the different fracture systems, and their frequency and possible connection with the main fault systems.

With the aim of subdividing the study area into homogeneous domains relative to the main morphostructural features (bedding attitude, shape of the slopes, main faults, lithological contrasts), we measured a total of 330 attitudes of fault planes and fractures in 7 sites, in different lithotypes at variable stratigraphic height (Figure 1). The collected data have been statistically analyzed to obtain information about their spatial distribution through the identification of fracture families (principal trends of fractures), which have been defined for each domain by plotting contoured stereo-net pole-frequency and normalized azimuth-frequency (rose) diagrams. A unimodal Gaussian curve-fitting routine is then used for determining peaks in directional data (DAISY software by *Salvini et al.*,

248 [1999]), from which the statistical parameters are derived. We report these results in Figure 2 for each
249 measurement site.
250 Almost all the measured features are subvertical, with angles of dip ranging between 70° and 90°. We
251 recognized four main fracture families both inside and outside the Solfatara crater, showing a relatively
252 small dispersal of the strike angle around the direction of the two main fault systems that border the
253 crater. N50W±25° and N50E±20° trending fractures form two pairs of conjugate systems, compatible
254 with the geometry of the main faults responsible for the quadrangular shape of the Solfatara crater
255 morphology. Although no kinematic indicators have been detected with the present survey, a normal
256 stress field, characterized by a subvertical σ1, subhorizontal NW-SE and NE-SW trending σ2 and σ3,
257 and R=(σ2- σ3)/(σ1-σ3)=0.18, as hypothesized by *Chiodini et al.* [2001], is consistent with our data.
258 Two subordinate N-S and E-W trending systems of fractures, on average characterized by slightly
259 lower angle of dip, ranging between 60° and 80°, have been measured along the high-angle inner
260 slopes of the Solfatara crater, which are affected by gravitational instability phenomena, evidenced by
261 rock falls and localized translational and rotational sliding of parts of the inward-dipping, stratified,
262 pyroclastic succession. These fractures have been here interpreted as surface deformations, produced to
263 accommodate the movement along the NW-SE and NE-SW fault systems, during the gravitational
264 readjustment of the inner-crater slopes.
265
266 **3.2. Seismic Array Deployment**
267 The seismic survey was carried out in April 2007, using Lennartz MarsLite seismic stations equipped
268 with three-component 1-Hz Mark LE3Dlite seismometers for the acquisition of seismic noise. We
269 installed a total of 5 seismic arrays labelled A, B, C, D and E, sampling different areas of the crater
270 (Figure 1). Arrays consisted of 4 sensors, set up with a circular geometry in which a sensor was placed
271 at the center and the remaining three at fixed radius and evenly spaced (120°) around the

circumference. Each day we deployed a single array whose configuration was changed by increasing the radius. Arrays A, B and D were designed with radii of 5, 10, 25, 50 and 100 m. Arrays C and E had radii of 5, 10 and 25 m. About 1-hour of seismic noise was recorded for each circular configuration with fixed radius and a total of 68 sites were sampled by each sensor. More details about acquisition and data format can be found in *Petrosino et al.* [2008]. Arrays A, D and E were located approximately in the central part of the crater, array B was deployed in the area of the Fangaia, while array C was placed to the north, near the crater rim and the fumarole area (Figure 1) . For each array configuration we calculated the "array transfer function" [*Rost and Thomas*, 2002] that represents the frequency-wavenumber spectrum in response to a vertical incident impulse. The array resolution in wavelength that is directly related to the geometry of the array (inter-station distance and aperture) was estimated from the array transfer function [*Di Giulio et al.*, 2006; *Wathelet et al.*, 2008]. The values of minimum (kmin/2) and maximum (kmax) resolvable wavelength are reported in Table 2 for each array configuration.

3.3. Background properties of seismic noise

We performed a preliminary study of seismic noise aimed at its spectral and temporal characterization, in order to verify if this signal is suitable for the H/V ratio and surface wave dispersion analyses, and to choose the proper parameters for the application of these techniques.

a) Nature of the Noise Source and Spectral Characteristics

Seismic noise at the Solfatara volcano has a predominant anthropogenic nature, as one can easily deduce by the time pattern of the root mean squared (RMS) noise amplitude filtered in the 1-20 Hz frequency band which clearly shows a 24h periodicity (Figure 3). RMS is calculated over a 1-hour long time window; daytime noise amplitude is about 3-4 times greater than that in the night-time. The data

used for the RMS analysis were recorded at SFT station (Figure 1), a permanent installation in the Solfatara crater of the Istituto Nazionale di Geofisica e Vulcanologia (INGV), equipped with a 3-component 1-Hz Mark LE3Dlite sensor. The analysed samples are relative to an entire week, from Monday to Sunday, in the period 2-8 April 2007. Similar results are obtained by changing the filter frequency band (1-15 and 1-10 Hz). Spectra of noise samples continuously recorded at SFT station show frequency peaks irregularly spread in the 2-20 Hz band. The same evidence was in found analyzing 1-hour-long noise samples recorded by 5 representative stations of the temporary arrays deployed within the Solfatara crater (see Figures 5-9 in *Petrosino et al.* [2008]).

b) Stationarity of Seismic Noise

Stationarity of the time series is a fundamental pre-requisite for the application of the present techniques. A check of this assumption is mandatory, as the analysis carried out on time series with a limited time duration. A first element to be addressed is the presence inside the Solfatara crater of many visitors during the day-time, producing transients and disturbances in the seismic recordings. In this condition it is particularly important to verify the stability of the H/V ratio in time, or, equivalently, to check that 1-hour-long recordings for each station can be considered a statistically representative sample of the entire process.

In order to check that hourly and daily cyclic variations of noise amplitude and frequency content, and the presence of transients do not affect the stability of the H/V ratio, we used data continuously recorded by the permanent station SFT. We calculated the H/V ratio over noise samples lasting 1 hour, acquired during the week when the seismic survey took place. Each 3-component recording was bandpass filtered in the 1-20 Hz frequency band and an STA/LTA algorithm (with a short-term average, STA, of 1s and a long-term average, LTA, of 30s) was applied in order to reject the most energetic transients and disturbances. Time-windows of 40s with an overlap of 30% were selected. The

320 Fourier spectra of the NS and EW components were geometrically averaged to obtain the horizontal
321 component Fourier spectrum and the spectral ratios between the horizontal and vertical components
322 smoothed by a Konno-Omachi function [*Konno and Omachi*, 1998] were calculated. Finally, the
323 arithmetic mean of all the H/V ratios over each hourly recording was calculated. Several tests were also
324 performed by changing the bandpass filter (1-15 Hz, 1-10 Hz), the window length (40-80s), the overlap
325 (20-40%) and the Konno-Omachi smoothing factor (40-60). All these tests yield similar and stable
326 results. We verified that number and length of the selected time windows ensure the reliability of the
327 H/V curve according to the criteria defined in the SESAME European Project Deliverable D23.12
328 (available from http://sesame-fp5.obs.ujf-grenoble.fr). Moreover, we also checked that the obtained
329 H/V peak verifies the amplitude and stability conditions indicated in the above-cited report, for an
330 unambiguous and correct identification of the resonance frequency.
331 In Figure 4 we show the 168 H/V spectral ratios relative to the period 2-8 April 2007 calculated for the
332 SFT site: the fundamental frequency at about 4.4 Hz and the average peak amplitude of about 12 are
333 stable for all the analysed period. Slightly variations of these quantities occur within the standard
334 deviation interval, which corresponds to errors on the order of 5-10% for the frequency values and of
335 about 10% for the peak amplitudes.
336

337 **3.4. Horizontal-to-Vertical Analysis of Array Data**

338 The H/V spectral ratios were calculated for all the recording points sampled by the 5 arrays by using
339 the procedure and the parameters previously described for the permanent station SFT. As we have
340 already stated, the seismic noise recordings at the Solfatara crater often contain many transients due to
341 the presence of the numerous tourists that visit the volcano daily. Therefore a careful check of the
342 influence of non-stationary noise on the H/V ratios was performed by using both the raw seismograms
343 and an STA/LTA algorithm to reject disturbances. The comparison of the obtained results show no

differences in the resonance frequencies and peak amplitudes calculated in both the ways. This is in agreement with the observations and the numerical simulations published by *Parolai and Galiana-Merino* [2006] which show that transients have no (or little) effect on the H/V ratio. The reliability of the obtained H/V spectral curves and the significance of the retrieved resonance frequencies and peak amplitudes were checked according to the criteria of the SESAME European Project Deliverable D23.12 (available from http://sesame-fp5.obs.ujf-grenoble.fr): all the H/V ratios calculated for the array stations passed the tests. The associated errors are on the order of 5-10% for the frequency values and of about 5-15% for the peak amplitude values. A map (Figure 5) of the resonance frequencies and peak amplitudes was obtained by applying an inverse-distance-to-a-power gridding method that interpolates the H/V data such that the influence of one point relative to another declines with distance from the grid node. In the interpolation procedure we assumed the validity of the H/V ratio over a circle of radius of 30 m. Frequency values relative to the different sampled sites range from 3.6 to 7 Hz. The central and southern parts of the crater, corresponding to the arrays A, B, D and E are characterized by similar values of resonance frequencies (in the 4-5 Hz band), except for the station DR51 located near the inner crater slopes and station BR43 close to the Fangaia mud pool, that show higher values of frequency (6.2 and 7 Hz, respectively). Higher frequencies compared to the average value (from 5.4 up to 7 Hz) are also observed in the northern part, beneath most of the sensors of array C located near the inner crater slopes.

As regards the H/V peak amplitudes, we observe that the Fangaia area, corresponding to array B, shows low values ranging from 2.5 to 5, with exception of stations BR42 and BR52 that fall outside the mud pool area and have slightly higher amplitudes. The part of the crater to the north of the Fangaia, exhibits higher peak amplitudes, with values ranging from 7 to 15. The area where array D is set up shows a highly heterogeneous behaviour: the H/V amplitudes at the northern stations (DR53, DR43 and DR33) are comparable with those that characterize the central and northern part of the crater, while

368 high peak values (up to 24) are observed in correspondence of the central stations (DR11, DR21,
369 DR32, DR31). Moreover, for the eastern station DR51 we obtain a low peak amplitude, comparable to
370 those of the Fangaia area.
371
372 **3.5. Dispersion Curves Estimates**
373 We assumed that the vertical motion component of noise wavefield (in the frequency range we
374 considered) at the Solfatara is dominated by Rayleigh waves. This is justified by the observation that
375 the origin of high frequency seismic noise is mainly related to anthropogenic activity (as shown in
376 Section 3.3) and therefore the sources are mostly located at the surface [*Bonnefoy-Claudet*, 2004].
377 Under this hypothesis, we used three different methods to estimate the dispersion curves of Rayleigh
378 waves propagating through the array: the Frequency–Wavenumber (f-k) technique [*Lacoss et al.*,
379 1969], the Spatial Autocorrelation (SPAC) technique [*Aki*, 1957] and its modification (MSPAC)
380 proposed by *Bettig et al.* [2001].
381
382 *a) Frequency-Wavenumber Analysis*
383 In the f-k method the power spectral density is calculated as:
384 $\mathbf{P}(\mathbf{k},\omega)=\mathbf{e}^{H}(\mathbf{k})\mathbf{R}(\omega)\,\mathbf{e}(\mathbf{k})$ (1)
385 where $\mathbf{k}=(kx, ky)$ is the wavenumber vector, ω is the angular frequency, $\mathbf{R}(\omega)$ is the cross-spectral
386 matrix, $\mathbf{e}(\mathbf{k})$ is the steering vector containing the phase shift and $\mathbf{e}^{H}(\mathbf{k})$ is its Hermitian conjugate. The
387 maximum of the spectral estimator at a given frequency is searched in the wavenumber plane (kx, ky)
388 and the corresponding wavenumber vector is used to calculate the horizontal slowness (the inverse of
389 the apparent velocity):
390 $s(\omega)=|\mathbf{k}|/\omega$ (2)
391 In order to apply the f-k technique we bandpass filtered the 1-hour long recordings (vertical

component) in the 1-15 Hz range, choosing values of center frequency, *fc*, with the step of 0.1 Hz and bandwidth defined as 0.9*fc* - 1.1*fc*. The time window was selected equal to 30 times the central period of the analysed band, and the overlap between successive windows was set to 30%. For each frequency band, the f-k spectrum was computed over a grid with size equal to kmax and step less than kmin/4 (Table 2). The maximum corresponds to the best slowness value. A histogram of the slowness obtained for all the selected time-windows at a fixed frequency was constructed in order to calculated the mean value and its associated statistical error [*Ohrnberger et al.*, 2004].

The phase velocity dispersion curve of the fundamental mode of Rayleigh waves was obtained for each array by plotting the velocity values as a function of frequency and selecting the part of the curve bounded by the resolution limits defined through kmin and kmax (Table 2). Actually, each array configuration with fixed radius defines the dispersion pattern in a limited frequency band: the smaller the radius, the higher the frequency range for which the dispersion branch is valid. Therefore, the total dispersion over the whole frequency band of 1-15 Hz was finally obtained by joining the 5 dispersion curves (or 3 in case of array C and E) estimated for each configuration with fixed radius (Figure 6). The phase velocity ranges from 100 m/s at high frequency to about 1000 m/s at frequency of 2 Hz. Phase velocity values are well retrieved from 15 Hz down to 4.5-5 Hz (which roughly corresponds to the average H/V peak estimated from Nakamura's technique [*Nakamura*, 1989]), while below 5 Hz velocity data are more scattered. This could be due to the increasing loss of coherency with the increasing array aperture (particularly evident for radii equal to 50 and 100 m). Moreover some authors have pointed out the difficulty to obtain the part of the dispersion curve just below the resonance frequency of a site [*Di Giulio et al.*, 2006; *Wathelet et al.*, 2008 and references therein]. Comparing the dispersion curves for the 5 arrays one can note that at least for frequencies greater than 5 Hz, the array C (the northern one) is characterized by higher velocities with respect to those of the arrays A, D and E located in the central part of the crater. On the other hand, the array B deployed in the Fangaia area

shows intermediate values. Below 5 Hz, these differences in the phase velocity values are no longer appreciable.

b) SPAC and MSPAC Analyses

For an array of receivers in a circular configuration, *Aki* [1957] demonstrated that the phase velocity, for signals on the vertical component and filtered in a narrow frequency band around the ω_0, can be obtained by fitting a zeroth-order Bessel function, to the azimuthal average of the spatial correlation coefficients, $\bar{\rho}(r,\omega_0)$, according to:

$$\bar{\rho}(r,\omega_0) = J_0\left[\frac{\omega_0}{c(\omega_0)} r\right] \qquad (3)$$

with r the radius of the array, J_0 the zeroth-order Bessel function and $c(\omega_0)$ the phase velocity.

Extension of Aki's SPAC method toa non-circular array [*Bettig et al.*, 2001] consists in averaging, for each individual target frequency, the correlation coefficients evaluated at subsets of M station pairs whose distances range between r-dr and r+dr. A generic configuration can be then reviewed as a family of concentric rings. In such a frame, equation (1) becomes:

$$\bar{\rho}_{r_1 r_2}(\omega_0) = \frac{2}{r_2^2 - r_1^2} \frac{c(\omega_0)}{\omega_0} \left[r_2 J_1\left(\frac{\omega_0 r_2}{c(\omega_0)}\right) - r_1 J_1\left(\frac{\omega_0 r_1}{c(\omega_0)}\right)\right] \qquad (4)$$

where J_1 is the first-order Bessel function.

We applied both the classical and modified SPAC (MSPAC) methods, using the same parameters to calculate the average correlation coefficients. Since the final results are similar and the errors associated to the MSPAC dispersion curves are significantly smaller, we decided to illustrate only MSPAC analysis.

Considering all the possible station pairs, we arranged a set of 2 rings, each containing 3 station pairs

for every array configuration. As for the f-k analysis, we filtered the vertical component of 1-hour-long signals in the band 1-15 Hz. For each ring, we used 60-s-long time windows with an overlap of 30%, to calculate the average correlation coefficient. The obtained series, containing 100 samples linearly spaced over 1-15 Hz frequency band, were used to fit equation (4). The Rayleigh wave fundamental mode dispersion curves, $c(\omega_0)$, were obtained by picking the maxima of the semblance function, calculated in the fitting procedure, in the slowness-frequency plane. The frequency range of the dispersion curves for each configuration is determined by the resolution limits kmin and kmax (Table 2). The error associated with the dispersion at a given frequency value is calculated by the spreading of the semblance maxima corresponding to that frequency. The total dispersion curve for each array is finally obtained with the same procedure used in f-k method (Figure 7). The dispersion curves retrieved from MSPAC and f-k methods are comparable. Therefore all the general observations made for f-k curves hold, although the dispersion patterns obtained by the MSPAC technique are less scattered below 5 Hz. Since the MSPAC curves are affected by smaller errors, they were chosen to be inverted for the S-wave velocity model.

3.6. Dispersion Curve Inversion

For each array we inverted the dispersion curves obtained from MSPAC analysis, jointly with the corresponding average H/V resonance frequency, whose value depends on the layer thickness and the shear-wave velocity [*Kramer*, 1996] and therefore can be used as a constraint in the inversion procedure. In order to obtain the 1-D S-wave velocity profiles we used the neighbourhood algorithm [*Sambridge*, 1999] as implemented by *Wathelet et al.* [2004, 2005, 2008]. This algorithm performs a stochastic search over the parameter space, defined by S- and P-wave velocities, top depths, densities and Poisson's ratios of the subsurface layers. The goodness of results is evaluated through minimizing misfit function, defined as:

$$misfit = \sqrt{\sum_{i=1}^{n_F} \frac{(x_{di} - x_{ci})^2}{\sigma_i^2 n_F}} \qquad (5)$$

where x_{di} and x_{ci} are the experimental and theoretical velocity, respectively, at frequency f_i, σ_i is the uncertainty of the considered frequency sample, n_F is the number of frequency samples at frequency f_i. The inversion of dispersion data is a non-unique problem, i.e. several velocity profiles can be retrieved from the same dispersion curve by using different parameterizations, in particular the number of layers and the half space depth. To overcome this difficulty we evaluated the misfit value over a wide range of parameterizations and for each one we performed a set of 5 inversions to check the robustness of the results [*Di Giulio et al.*, 2012]. For each array and each parameterization we obtained a set of 5 best models with associated 5 minimum misfit values. Then, to select the most likely velocity profile, we analyzed the behaviour of the minimum misfit as the parameterization varies, taking into account that: a) the minimum misfit as a function of the number of layers reaches a minimum in correspondence of the more realistic number of layers [*Renalier et al.*, 2010; *Di Giulio et al.*, 2012]; b) the half space depth increases with the number of layers and starts to scatter around the actual depth [*Renalier et al.*, 2010]. We illustrate these behaviours in Figure 8; on the left, the minimum misfit shows a clear minimum in correspondence of 2 layers for the array A and C, 3 for array B and 1 for array E; on the right, the corresponding half space depth can be easily identified. The behaviour of the array D is ambiguous. Although an absolute minimum for the minimum misfit can be recognized, none of the parameterizations inside the range 2-4 number of layers dominates (green triangles in Figure 8, on the left). The final profile ensembles for each array were obtained in correspondence of the previous minima and they are plotted in Figure 9, where the most likely S-wave profiles are shown in the central panels. On the left we show the theoretical dispersion curves for the Rayleigh fundamental mode and the experimental ones, with the respective error bars. A good agreement is obtained for the array A, B,

C and E. The mismatch occurred for the array D is to be attributed to a poorly constrained depth for the second layer. The right panel of the Figure 9 reports the theoretical ellipticity curves, calculated for the velocity profiles, that fit the H/V peaks inside the standard deviations (grey vertical bars).

Since our final goal is to retrieve a shallow 3-D S-wave velocity model for the Solfatara crater by combining the results obtained from the inversion procedure, we estimated the statistical level of significance associated to each depth and velocity of the 5 1-D profiles by using a Monte Carlo algorithm. We generated 100 random dispersion curves inside the error bars for each array and inverted them following the same procedure previously described. This procedure constitutes a test which quantifies how well the inversion algorithm reconstructs synthetic models when the dispersion curves are perturbed. The obtained mean velocity profiles and their associated standard deviations are shown Figure 9 (black continuous and dashed lines, respectively, in the central panels) superimposed to the velocity profile ensembles A first consideration on these results is that the mean profiles coincide with the best 1-D profiles, confirming the goodness of the inversion procedure and the Gaussian structure of the errors. The errors on the velocity in the first 12 meters of depth, calculated with MonteCarlo method are at most of the order of 10 percent of the estimate. This evidence suggests that the procedure utilized is sensitive to the crustal heterogeneity (vertical and horizontal) close to the surface. Conversely, resolution decreases as depth increases. Finally, the D array shows a low precision (53%) in the determination of the subsurface structure under the hypothesis of parallel-plane layers (with constant velocity) at intermediate depths. Although poorly constrained, this velocity structure is indicative of the average properties of the medium beneath the array D.

In order to obtain a 3-D velocity model corresponding to the volume below the 5 arrays, we applied a inverse-distance-to-a-power gridding method to the 5 mean 1-D velocity profiles. The velocity data are weighted during the interpolation process, such that the influence of one point relative to another declines with distance from the grid node coincident with the array centers. For the generation of the

grids we used circular domains with the same geometrical dimension of the corresponding array, leaving the zone without data as blank. We performed the following resolution tests to ensure that the algorithm does not introduce artificial patterns in the velocity spatial distribution. 1) All the volume is set at a uniform velocity. 2) In turn, one model underneath one array, is left unchanged and the remaining volume is set at a uniform velocity. 3) In turn, one model underneath one array, is slightly varied and the other four models remain unchanged. All the tests do not show spurious patterns. It has to be said that our 3-D model preserves the good original vertical resolution of the 1-D profiles, while the position of the horizontal velocity discontinuities are only constrained by the array aperture since the 1-D models do not carry information about their horizontal extent.

In Figure 10 we show the S-wave velocity horizontal slices at the different depths. A wide spatial variability of the velocity between 0 m (station plane) and 12 m depth is retrieved (Figure 10 a-e). In the range 0-5.0 m (Figure 10a) we can distinguish the velocity variation from 120 m/s for the eastern part of the crater (array A and D) to 200 m/s for the western part. Then an increase of the S-wave velocity starts in the southern area at depths between 5.0 and 5.5 m (Figure 10b), involving also the northern sector in correspondence of depths 5.5-7.2 m (Figure 10c), where a maximum velocity of 400 m/s is reached beneath the array C. The lower velocity area remains confined in the central part of the crater. Between 7.2 and 12 m (Figure 10d) the velocity in the eastern area increases up to 650 m/s. At these depths the volume results divided in a higher velocity part (to the east, corresponding to the fumaroles below the array D) and a lower one (corresponding to the western edge below the array E), with a transition central zone. From 12 to 17 m (Figure 10e) the velocity increases up to 1300 m/s in the western area. Figure 10f shows the volume between 17-28 m with an increase up to 900 m/s of the velocity below the array B. Depths 28-40 m are represented in the panel g of Figure 10, where the higher velocity area in the north-western sector (up to 1400 m/s below the array C) bounds the centre of the crater, characterized by lower velocities (500 m/s) beneath the array A. The next two panels (h and

534 i) represent the volume, explored only by arrays A, B and D, below 40 m depth which is the limit of
535 resolution for the array E and C [*Midzi*, 2001]. The 60-150 m depths (Figure 10h) are characterized by
536 a higher velocity in the centre and north-east area, with values between 1000 and 1900 m/s, while
537 lower velocity corresponds to the array D (about 650 m/s). The final slice (below 150 m) that
538 represents the velocity values just above the limit of detection (about 200 m) for the array A, B and D,
539 shows a higher velocity (1700-1900 m/s) area in correspondence of the array A and B, and a lower
540 velocity region (1000 m/s) below the array D.
541
542 **3.7. Polarization Analysis**
543 We investigated the polarization properties of seismic noise by applying the covariance matrix method
544 [*Jurkevics*, 1988] to the three-component seismograms. Through a diagonalization procedure, the
545 following parameters are estimated:
546 1) the rectilinearity, defined as $RL= 1- (\lambda_2 + \lambda_3 /2\lambda_1)$, with $\lambda_1 > \lambda_2 > \lambda_3$ the eigenvalues of the
547 covariance matrix. RL takes values between 0 (pure spherical motion) and 1 (pure rectilinear motion);
548 2) the azimuth of the polarization vector. It is the angle between the projection on the horizontal plane
549 of the polarization vector and north, measured clockwise; and
550 3) the incidence angle between the polarization vector and the vertical axis.
551 The samples of seismic noise were filtered by applying a bandpass a-causal Butterworth filter in
552 different frequency ranges (1-10, 5-10, 5-15 Hz); polarization parameters were estimated using 1-s-
553 long sliding window with overlap of 50%. Similar polarization patterns were found independently of
554 the frequency band, therefore we discuss the results of the analysis in the 1-10 Hz range.
555 We selected the stations for which the distribution of RL has a 70% of values equal or greater than 0.5,
556 because in this case the angular parameters are associated with surface and body waves, while for RL
557 less than 0.5 they lose their significance. The incidence angles from the polarization analysis are in the

range 80°-90°, confirming the shallow propagation of the noise wavefield. Moreover, narrow azimuthal distributions of the polarization vector are shown in the rose diagrams of Figure 11. The representation in terms of the vectorial field (Figure 11) was obtained using the mean value of the azimuth for each site and applying an inverse-distance-to-a-power gridding method. The interpolation was limited to a circle of radius of 30 m around each station. The magnitude of the vectors was set proportional to the inverse of the standard deviation of the azimuth mean value. Results of the analysis evidence the tendency of ambient noise to be polarized. In the central and northern part of the crater, going from the west to the east, the horizontal polarization vector is first oriented NW-SE, then it seems to switch to a roughly N-S direction, and finally it assumes a E-W orientation. In particular, the array D is affected by the greatest inter-station variability of the azimuth of the polarization vector. In the Fangaia area, the azimuth retrieved for stations BR43, BR00 and BR52 shows a preferred orientation along the NW-SE direction, while station BR33 has a NE-SW polarization. However, this anomalous wave propagation occurs locally, beneath the station located just above the edge of the mud pool.

4. Discussion

In the present paper we combine the results obtained from seismic noise analysis with those from a volcanological and morphostructural study of the Solfatara volcano, in order to reconstruct the formation and evolution processes of the volcano and to model its shallow crustal structure. Figure 12 is an interpretative cross-section, based on the results of the volcanological, morphostructural and seismological investigations.

The volcanological features described in Section 3.1. suggest that the eruption that generated the Solfatara volcano was a complex and likely long-lasting event, during which a former crater (Crater 1; Figures 1 and 12) was formed during the early phreatomagmatic and magmatic explosions, which occurred in the area of the preexisting Mt. Olibano lava dome, generating the breccia deposits and the

582 lower part of the overlying pyroclastic sequence. The upper part of the sequence, which lies above the
583 uppermost angular unconformity, was generated by a series of phreatomagmatic explosions in the latest
584 stages of the Solfatara eruption, likely after a pause in the activity. Its thickness and grain-size
585 variations suggest a provenance from a smaller, ring-shaped vent area (Crater 2; Figures 1 and 12),
586 nested within the previous main crater. This eastward vent migration is likely controlled by the
587 intersection of the NW-SE and NE-SW trending fault systems that crosscut the Solfatara area, as
588 evidenced by the structural survey. The Solfatara area, located along the north-eastern boundary of the
589 La Starza resurgent block, is largely deformed by these two fault systems, and by the subordinate N-S
590 and E-W trending systems of fractures, that we interpreted as surface deformations, produced to
591 accommodate the movement along the main NW-SE and NE-SW fault systems, during the
592 gravitational readjustment of the differentially deformed blocks. Both internal and external slopes of
593 the volcano show rectilinear parts and triangular facets related to the deformation that occurred during
594 and after the eruption along these features. This deformation has also been evident during recent
595 bradyseismic events, when the opening of a NE-SW trending fracture occurred in the area of the
596 Fangaia mud pool [*Acocella et al.*, 1999; *Orsi et al.*, 1999; *Vilardo et al.*, 2010].
597 The intense volcanic and deformation activity has generated a complex volcanic edifice characterized
598 by high vertical and horizontal heterogeneity, due to the overlapping of nested craters (Figure 12),
599 which have been variably filled by heterogeneous reworked deposits, produced by the morphologic
600 evolution of the inner slopes of the Solfatara edifice. These deposits are thickest in the central part of
601 the main crater and progressively thin outward, draping the inner flanks of the edifice. The last
602 observation fits quite well with the results of H/V analysis that shows higher resonance frequency
603 values in the north-eastern part of the crater, approaching the internal crater slopes, when compared to
604 the central area. Moreover, the detected shear-wave velocities for the shallower layers are typical of
605 loose and unconsolidated pyroclastic deposits [*Nunziata et al.*, 1999].

606 Another interesting observation concerns the low peak amplitude values obtained from the H/V
607 analysis in the Fangaia area, here interpreted as due to the presence of deposits saturated by
608 hydrothermal fluids. This interpretation is supported by the results of electrical resistivity profiles
609 [*Bruno et al.*, 2007]. Indeed, as observed by some authors [*Yang and Sato*, 2000; *Yang*, 2006], ground
610 motion amplification (and thus the amplitude ratios) is significantly affected by the saturation
611 conditions of the medium.
612 Immediately below the shallow deposits, the shear-wave velocity modeling again shows the presence
613 of both vertical and horizontal discontinuities. In particular, the eastern sector corresponding to Crater 2
614 (Figures 1 and 12), is characterized by high velocity values, which are typical of lithified tuffs
615 [*Nunziata et al.*, 1999]. The observed values and the contrasts with the surrounding areas corroborates
616 the hypothesis of the presence at shallow depth of a small volcanic edifice, likely a tuff-cone, formed
617 during the phreatomagmatic activity of Crater 2, and emplaced above the sediments filling the Crater 1
618 (Figure 12). The lateral and vertical lithological and structural discontinuities, due to the superposition
619 of the products related to this multivent activity would be ultimately the cause of the observed spatial
620 variability in the H/V peak amplitudes. In addition the high heterogeneity of this sector of the crater
621 possibly affects the phase velocity array measurements [*Bodin and Maupin*, 2008], making inadequate,
622 at intermediate depths, the parallel-plane layers modeling and thus producing a less constrained
623 velocity structure.
624 At a greater depth, a complex high-velocity body has been observed in the north-western sector of
625 Crater 1 (Figures 10 and 12). The recorded horizontal and vertical velocity variations suggest the
626 presence of lithified bodies surrounded by soft sediments, which can be interpreted as lava bodies,
627 emplaced inside Crater 1 and later overlain by the soft and likely reworked sediments that fill the
628 crater.
629 The deepest volume explored by the seismic arrays is characterized by the highest velocity values in

630 the central part of the Solfatara volcano, and by slightly lower values towards east, in the Fumarole
631 sector. This is also in agreement with the presence of lava bodies within the larger and older Crater 1,
632 and tuffs within Crater 2. Velocity values increase with depth, likely due to a generalized improvement
633 in the mechanical characteristics of the rocks.
634 The results of the morphostructural analysis of the Solfatara volcano evidence the interplay between
635 two conjugate N50W and N50E trending main fracture systems that define the geometry of the inner-
636 crater slopes, and two N-S and E-W trending subordinate systems, induced by the gravitational
637 readjustment of the slopes. This complex structural pattern could control the direction of the
638 polarization vector of seismic noise, as suggested by *Rigano et al.* [2008]. In fact a clear relationship
639 between the direction of the polarization vector and fault trend arises in the Fangaia area (Figures 1 and
640 11). Here the average azimuth shows a preferred orientation along a NW-SE direction, which is
641 approximately orthogonal to the trend of the main feature affecting this sector of the crater. Normal
642 polarization pattern could be consistent with the near-surface anisotropy or with a resonance
643 mechanism of seismic waves in the fault [*Rigano et al.*, 2008]. In the northern part of the Solfatara
644 crater, along an E-W profile the orientation of the horizontal polarization vector varies from roughly
645 orthogonal to parallel to the direction of the fractures. In this latter case the observed parallel pattern
646 could be interpreted in terms of fault-trapped surface waves and channeled in the waveguide [*Rovelli et*
647 *al.*, 2002; *Lewis et al.*, 2005]. However, due to the complex interplay among the variable fracture
648 systems in this part of the crater, their contribution to the noise polarization cannot be discriminated.
649 Moreover, the results could also be affected by the high degree of heterogeneity characterizing the local
650 lithology, and by the presence of the buried rim of Crater 2.
651

652 **5. Conclusions**

653 The Solfatara volcano has represented a good test-site to reconstruct the shallow crustal structure from

654 the application of different seismological techniques for the analysis of seismic noise, combined with
655 the results of volcanological and morphostructural investigations. In a sort of continuous feed-back
656 process, the surface geology of this area has been used to provide physical constraints needed for the
657 correct interpretation of spectral ratio resonance frequencies and peak amplitudes, S-wave velocity
658 model and polarization pattern, which in turn has led to constraints on the subsurface structure of the
659 volcano and its geological evolution.
660 At the Solfatara volcano, seismic noise has provided a great deal of information about the medium
661 properties whose knowledge is thus essential for seismologists, when a proper separation into source,
662 path and site effects is needed for a correct interpretation of volcanic earthquake source. This is
663 particularly important at this volcano, where long-period seismic events associated to the activity
664 hydrothermal system occur in the top 500 m [*Cusano et al.*, 2008].
665 The S-wave velocity structure inferred in the present study provides a detailed 3-D model for the
666 Solfatara subsurface down to a depth of about 200 m. Previous models calculate 1-D S-wave velocity
667 profiles from active seismic data, with a maximum resolution down to a depth of 32 m [*Bruno et al.*,
668 2007], or they represent an average 1-D profile for an area including not only the Solfatara volcano but
669 also the town of Pozzuoli [*Petrosino et al.*, 2006], hence with a lower spatial resolution compared to
670 the present results. Moreover our study confirms that, as observed by *Rigano et al.* [2008], polarization
671 of seismic noise is sensitive to the presence of faults and could be indicative of the orientation of the
672 fracture systems. In the future, this interesting result could be further improved by replacing single
673 stations with very small arrays, in order to perform array-averaged polarization measurements.
674 The joint interpretation of the S-wave velocity model, together with the results of the polarization
675 analysis and the volcanological and morphostructural observations, contributes not only to imaging the
676 shallow crustal structure of the volcano at a small scale, but also to put some constraints on its
677 geological evolution. A new evolutionary model of the Solfatara volcano in which the volcano has been

characterized by a long-lasting multivent activity, due to vent migration along structurally-controlled fissures. The geometry of at least two tuff-cone craters, later intruded by viscous lava domes and filled by tephra and reworked sediments, is clearly shown by both the geological and seismological survey carried out with this study.

The outcomes presented in our paper improve the knowledge of the Solfatara volcano, thus contributing to evaluate and assess volcanic hazard in a densely populated area like the Campi Flegrei volcanic complex, and to support further geophysical and volcanological researches. These outcomes should encourage new surveys at active volcanoes and to adopt such a multidisciplinary approach.

Acknowledgments

The Administration of the Solfatara Volcano is acknowledged for having allowed us to deploy the seismic instruments in the Naturalistic Park. We wish to thank Mariacira Veneruso, Lucia Zaccarelli and Vincenzo Torello who greatly helped us in the field work, and Francesca Bianco and Roberto Scarpa for their useful suggestions. Bill Fry, Catherine Lewis Kenedi and an anonymous Reviewer are acknowledged for their comments that helped us in improving the manuscript. Most part of data analysis was done by using Geopsy and Dinver software (available from http://www.geopsy.org/). This work was carried out in the framework of the projects entitled ‘SPeeD’ and ‘UNREST’ (Civil Defence of Italy and the Istituto Nazionale di Geofisica e Vulcanologia), and PRIN (Italian Ministry of Education). Data and results of preliminary analyses are fully available upon request to simona.petrosino@ov.ingv.it.

References

Acocella, V., F. Salvini, R. Funiciello, and C. Faccenna (1999), The role of transfer structures on volcanic activity at Campi Flegrei (Southern Italy), *J. Volcanol. Geotherm. Res.*, 91, 123–139, doi:10.1016/S0377-0273(99)00032-3.

Aki, K. (1957), Space and time of stationary stochastic wave, with special reference to microtremors, *Bull. Earthq. Res. Inst. Univ. Tokyo*, 35, 415-457.

Aki, K. (1965), A note on the use of microseisms in determining the shallow structure of the Earth's crust, *Geophysics, 30*, 665– 666, doi:10.1190/1.1439640.

Alfaro, A., L.G. Pujades, X. Goula, T. Susagna, M. Navarro, J. Sánchez, and J. A. Canas (2001), Preliminary map of soil's predominant periods in Barcelona using microtremors, *Pure Appl. Geophys., 158*, 2499-2511, doi:10.1007/PL00001182.

Amato, A., and P. Montone (1997), Present-day stress field and active tectonics in southern peninsular Italy, *Geophys. J. Int., 130*, 519-534, doi: 10.1111/j.1365-246X.1997.tb05666.x.

Battaglia, J., C. Troise, F. Obrizzo, F. Pingue, and G. De Natale (2006), Evidence of fluid migration as the source of deformation at Campi Flegrei caldera (Italy), *Geophys. Res. Lett., 33*, L01307, doi:10.1029/2005GL024904.

Battaglia, J., A. Zollo, J. Virieux, and D. Dello Iacono (2008), Merging active and passive data sets in traveltime tomography: The case study of Campi Flegrei caldera (southern Italy), *Geophys. Prospect., 56*, 555–573, doi: 10.1111/j.1365-2478.2007.00687.x.

Bean, C.J., I. Lokmer, and G. S. O'Brien (2009), Moment tensor inversion of Long Period signals: The effect of near surface velocity structure, in *VOLUME: VOLcanoes, Understanding subsurface mass moveMEnt,* edited by C. J. Bean, A. K. Braiden, I. Lokmer, F. Martini, and G. S. O'Brien, VOLUME Consortium/Jaycee Printing, Dublin.

Ben-Zion, Y., Z. Peng, D. Okaya, L. Seeber, J. G. Armbruster, N. Ozer, A. J. Michael, S. Baris, and M.

726 Aktar (2003), A shallow fault-zone structure illuminated by trapped waves in the Karadere-Duzce
727 branch of the North Anatolian Fault, western Turkey, *Geophys. J. Int., 152,* 699–717,
728 doi:10.1046/j.1365-246X.2003.01870.x.
729 Bettig, B., P.-Y. Bard, F. Scherbaum, J. Riepl, F. Cotton, C. Cornou and D. Hatzfeld (2001), Analysis
730 of dense array noise measurements using the modified spatial auto-correlation method (SPAC).
731 Application to the Grenoble area, *Boll. Geof. Teo. Appl., 42,* 281-304.
732 Bianco, F., E. Del Pezzo, G. Saccorotti, and G. Ventura (2004), The role of hydrothermal fluids in
733 triggering the July-August 2000 seismic swarm at Campi Flegrei, Italy: evidence from
734 seismological and mesostructural data, *J. Volcanol. Geotherm. Res., 133,* 229–246, doi:
735 10.1016/S0377-0273(03)00400-1.
736 Bodin, T., and V. Maupin (2008), Resolution potential of surface wave phase velocity measurements at
737 small arrays, *Geophys. J. Int., 172,* 698–706. doi: 10.1111/j.1365-246X.2007.03668.x.
738 Bonnefoy-Claudet, S. (2004), Nature du bruit de fond sismique: implication pour les études des effets
739 de site. PhD thesis, Université Joseph Fourier (LGIT), Grenoble, France.
740 Bonnefoy-Claudet, S., C. Cornou, P.-Y. Bard, F. Cotton, P. Moczo, J. Kristek, and D. Fäh (2006), H/V
741 ratio: a tool for site effects evaluation. Results from 1-D noise simulations, *Geophys. J. Int., 167,*
742 827–837, doi: 10.1111/j.1365-246X.2006.03154.x.
743 Bozdag, E., and A. Kocaoglu (2005), Estimation of site amplifications from shear-wave velocity
744 profiles in Yesilyurt and Avcilar, Istanbul, by frequency-wavenumber analysis of microtremors, *J.*
745 *Seismol., 9*, 87-98, doi: 10.1007/s10950-005-5271-8.
746 Bruno, P. P. G., G. P. Ricciardi, Z. Petrillo, V. Di Fiore, A. Troiano, and G. Chiodini (2007),
747 Geophysical and hydrogeological experiments from a shallow hydrothermal system at Solfatara
748 Volcano, Campi Flegrei, Italy: Response to caldera unrest, *J. Geophys. Res., 112,* B06201,
749 doi:10.1029/2006JB004383.

750 Cesca, S., J. Battaglia, T. Dahm, E. Tessmer, S. Heimann, and P. Okubo (2008), Effects of topography
751 and crustal heterogeneities on the source estimation of LP event at Kilauea volcano, *Geophys. J.*
752 *Int., 172,* 1219-1236, doi: 10.1111/j.1365-246X.2007.03695.x.
753 Chiodini, G., F. Frondini, C. Cardellini, D. Granieri, L. Marini, and G. Ventura (2001), CO_2 degassing
754 and energy release at Solfatara volcano, Campi Flegrei, Italy, *J. Geophys. Res., 106,* 16213–
755 16221, doi: 10.1029/2001JB000246.
756 Chouet, B., G. De Luca, P. Dawson, G. Milana, M. Martini and R. Scarpa (1998), Shallow velocity
757 structure of Stromboli Volcano, Italy, derived from small aperture array measurements of
758 strombolian tremor, *Bull. Seismol. Soc. Am., 88,* 653-666.
759 Cusano, P., S. Petrosino, and G. Saccorotti (2008), Hydrothermal origin for sustained long-period (LP)
760 activity at Campi Flegrei Volcanic Complex, Italy, *J. Volcanol. Geotherm. Res., 177,* 1035-1044,
761 doi:10.1016/j.jvolgeores.2008.07.019.
762 D'Auria, L., F. Giudicepietro, I. Aquino, G. Borriello, C. Del Gaudio, D. Lo Bascio, M. Martini, G. P.
763 Ricciardi, P. Ricciolino, and C. Ricco (2011), Repeated fluid-transfer episodes as a mechanism for
764 the recent dynamics of Campi Flegrei caldera (1989–2010), *J. Geophys. Res., 116,* B04313,
765 doi:10.1029/2010JB007837.
766 De Natale, G., G. Innaccone, M. Martini, and A. Zollo (1987), Seismic sources and attenuation
767 properties at the Campi Flegrei volcanic area, *Pure Appl. Geophys., 126,* 833-917.
768 De Siena, L., E. Del Pezzo, and F. Bianco (2010), Seismic attenuation imaging of Campi Flegrei:
769 Evidence of gas reservoirs, hydrothermal basins, and feeding systems, *J. Geophys. Res., 115,*
770 B09312, doi:10.1029/2009JB006938.
771 de Vita, S., G. Orsi., L. Civetta, A. Carandente, M. D'Antonio, T. Di Cesare, M. Di Vito, R.V. Fisher,
772 R. Isaia, E. Marotta, M. Ort, L. Pappalardo, M. Piochi, and J. Southon (1999), The Agnano-Monte
773 Spina eruption (4,100 years BP) in the restless Campi Flegrei caldera (Italy), *J. Volcanol.*

774 *Geotherm. Res., 91,* 269-301, doi: 10.1016/S0377-0273(99)00039-6.
775 de Vita S., Orsi G., Di Vito M., Marotta E., Sansivero F. (2005), The role of pre-existing tectonic
776 structures on the geometry of calderas and resurgent blocks: a review. *Acta Vulcanologica, 17*, 9-
777 22.
778 Di Giulio, G., C. Cornou, M. Ohrnberger, M. Wathelet, and A. Rovelli (2006), Deriving Wavefield
779 Characteristics and shear-velocity profiles from two-dimensional small-aperture arrays analysis of
780 ambient vibrations in a small-size alluvial basin, Colfiorito, Italy, *Bull. Seismol. Soc. Am., 96,*
781 1915-1933, doi:10.1785/0120060119.
782 Di Giulio, G., A. Savvaidis, M. Ohrnberger, M. Wathelet, C. Cornu, B. Knapmeyer-Endrun, F.
783 Renalier, N. Theodoulidis, and P.-Y. Bard (2012), Exploring the model space and ranking a best
784 class of models in surface-wave dispersion inversion: Application at European strong-motion sites,
785 *Geophysics, 77*, B147, doi:10.1190/geo2011-0116.1.
786 Di Vito, M. A., L. Lirer, G. Mastrolorenzo, and G. Rolandi (1987), The Monte Nuovo eruption (Campi
787 Flegrei, Italy), *Bull. Volcanol., 49*, 608-615, doi: 10.1007/BF01079966.
788 Di Vito, M. A., R. Isaia, G. Orsi, J. Southon, S. de Vita, M. D'Antonio, L. Pappalardo, and M. Piochi
789 (1999), Volcanism and deformation since 12,000 years at the Campi Flegrei caldera (Italy), *J.*
790 *Volcanol. Geotherm. Res., 91*, 221-246, doi: 10.1016/S0377-0273(99)00037-2.
791 Di Vito, M. A., I. Arienzo, G. Braia, L. Civetta, M. D'Antonio, V. Di Renzo, and G. Orsi (2011), The
792 Averno 2 fissure eruption: a recent small size explosive event at the Campi Flegrei caldera (Italy),
793 *Bull. Volcanol., 73, 295-320*, doi: 10.1007/s00445-010-0417-0.
794 Dziewonski, A., and A. L. Hales (1972), Numerical analysis of dispersed seismic waves, *Meth.*
795 *Comput. Phys., 11*, 39–85.
796 Ekström, G., J. Tromp, and E. W. F. Larson (1997), Measurements and global models of surface wave
797 propagation, *J. Geophys. Res, 102*, 8137–8157, doi:10.1029/96JB03729.

798 Faccenna, C., Funiciello, R., Bruni, A., Mattei, M., Cagnotti, L. (1994), Evolution of a transfer related
799 basin: the Ardea basin (Latium, Central Italy). *Basin Research, 6,* 35-46, doi: 10.1111/j.1365-
800 2117.1994.tb00073.x.
801 Falanga, M., and S. Petrosino (2012), Inferences on the source of long-period seismicity at Campi
802 Flegrei from polarization analysis and reconstruction of the asymptotic dynamics, *Bull. Volcanol.*,
803 in press, doi:10.1007/s00445-012-0612-2.
804 Granieri, D., R. Avino, and G. Chiodini (2010), Carbon dioxide diffuse emission from the soil: ten
805 years of observations at Vesuvio and Campi Flegrei (Pozzuoli), and linkages with volcanic
806 activity, *Bull. Volcanol., 72,* 103-118, doi:10.1007/s00445-009-0304-8.
807 Isaia, R., M. D'Antonio, F. Dell'Erba, M. Di Vito, and G. Orsi (2004), The Astroni volcano: the only
808 example of closely spaced eruptions in the same vent area during the recent history of the Campi
809 Flegrei caldera (Italy), *J. Volcanol. Geotherm. Res., 133,* 171-191, doi: 10.1016/S0377-
810 0273(03)00397-4.
811 Isaia, R., P. Marianelli, and A. Sbrana (2009), Caldera unrest prior to intense volcanism in Campi
812 Flegrei (Italy) at 4.0 ka B.P.: Implications for caldera dynamics and future eruptive scenarios,
813 *Geophys. Res. Lett., 36,* L21303, doi:10.1029/2009GL040513.
814 Jurkevics, A. (1988), Polarization analysis of three component array data, *Bull. Seismol. Soc. Am., 78,*
815 1725– 1743.
816 Konno, K., and T. Ohmachi (1998), Ground motion characteristics estimated from spectral ratio
817 between horizontal and vertical components of microtremor, *Bull. Seism. Soc. Am. 88,* 228–241.
818 Kramer, S.L. (1996), *Geotechnical earthquake engineering*, Prentice Hall Inc., Upper Saddle River,
819 New Jersey.
820 Lacoss, R. T., E. J. Kelly, and M. N. Toksoz (1969). Estimation of seismic noise structure using arrays,
821 *Geophysics, 34*, 21–38, doi:10.1190/1.1439995.

822 Lewis, M. A., Z. Peng, Y. Ben-Zion, and F. L. Vernon (2005), Shallow seismic trapping structure in
823 the San Jacinto fault zone near Anza, California, *Geophys. J. Int., 162,* 867–881,
824 doi:10.1111/j.1365-246X.2005.02684.x.
825 Li, Y. G., K. Aki, D. Adams, and A. Hasemi (1994), Seismic guided waves in the fault zone of the
826 Landers, California, earthquake of 1992, *J. Geophys. Res., 99,* 11,705–11,722,
827 doi:10.1029/94JB00464.
828 Liotta, D. (1991), The Arbia-Val Marecchia line, Northern Apennines. *Ecl. Geol. Helv., 84,* 413-430.
829 Lokmer, I., and C. J. Bean, (2010), Properties of the near-field term and its effect on polarisation
830 analysis and source locations of long-period (LP) and very-long-period (VLP) seismic events at
831 volcanoes, *J. Volcanol. Geotherm. Res., 192,* 35-47, doi: 10.1016/j.jvolgeores.2010.02.008.
832 Luzon, F., Z. Al Yuncha, F. J. Sanchez-Sesma, and C. Ortiz-Aleman (2001), A numerical experiment
833 on the horizontal to vertical spectral ratio in flat sedimentary basins, *Pure Appl. Geophys., 158,*
834 2451-2461, doi: 10.1007/PL00001179.
835 Malischewsky P. G., and F. Scherbaum (2004) Love's formula and H/V-ratio (ellipticity) of Rayleigh
836 waves, *Wave Motion, 40,* 57-67, doi: 10.1016/j.wavemoti.2003.12.015.
837 Maresca, R., D. Galluzzo, and E. Del Pezzo (2006), H/V spectral ratios and array techniques applied to
838 ambient noise recorded in the Colfiorito Basin, Central Italy, *Bull. Seismol. Soc. Am., 96,* 490-505,
839 doi: 10.1785/0120050057.
840 Métaxian, J. P., P. Lesage, and J. Dorel (1997), Permanent tremor of Masaya Volcano, Nicaragua:
841 Wave field analysis and source location, *J. Geophys. Res., 102,* 22,529–22,545,
842 doi:10.1029/97JB01141.
843 Midzi, V. (2001), 3-D surface wave group velocity distribution in Central-Southern Africa, *J. Seismol.,*
844 *5,* 559-574, doi: 10.1023/A:1012027216142.
845 Mora, M., Ph. Lesage, B. Valette, G. Alvarado, C. Leandro, J.-Ph. Métaxian, and J. Dorel (2006),

Shallow velocity structure and seismic site effects at Arenal volcano, Costa Rica. *J. Volcanol. Geotherm. Res., 152,* 121-139, doi: 10.1016/j.jvolgeores.2005.09.013.

Nakamura, Y. (1989), A method for dynamic characteristics estimation of subsurface using microtremor on the ground surface, *Q. Rept. Railw. Tech. Res. Inst., 30,* 25–30.

Nunziata, C., R. Mele, and M. Natale (1999), Shear wave velocities and primary influencing factors of Campi Flegrei-Neapolitan deposits, *Eng. Geol., 54,* 299-312, doi: 10.1016/S0013-7952(99)00044-7.

Ohrnberger, M., E. Schissele, C. Cornou, S. Bonnefoy-Claudet, M. Wathelet, A. Savvaidis, F. Scherbaum, and D. Jongmans (2004), Frequency wavenumber and spatial autocorrelation methods for dispersion curve determination from ambient vibration recordings, in Proc. of 13th World Conf. on Earthquake Engineering, Vancouver, BC, Canada.

Orsi, G., S. de Vita, and M. Di Vito (1996), The restless, resurgent Campi Flegrei nested caldera (Italy): constraints on its evolution and configuration, *J. Volcanol. Geotherm. Res., 74,* 179-214, doi: 10.1016/S0377-0273(96)00063-7.

Orsi, G., L. Civetta, C. Del Gaudio, S. de Vita, M.A. Di Vito, S. M. Petrazzuoli, G. Ricciardi, and C. Ricco (1999), Short-term ground deformations and seismicity in the resurgent Campi Flegrei caldera (Italy): an example of active block-resurgence in a densely populated area. *J. Volcanol. Geotherm. Res., 91,* 415-451, doi: 10.1016/S0377-0273(99)00050-5.

Orsi, G., M.A. Di Vito, J. Selva, and W. Marzocchi (2009), Long-term forecast of eruption style and size at Campi Flegrei caldera (Italy), *Earth and Planetary Science Letters, 287,* 265-276, doi: 10.1016/j.epsl.2009.08.013.

Parolai, S., S. M. Richwalski, C. Milkereit, and P. Bormann (2004), Assessment of the stability of H/V spectral rations from ambient noise and comparison with earthquake data in the Cologne area (Germany), *Tectonophysics, 390,* 57–73, doi: 10.1016/j.tecto.2004.03.024.

870 Parolai S. and J. J. Galiana-Merino (2006), Effect of transient seismic noise on estimates of H/V
871 spectral ratios, *Bull. Seismol. Soc. Am., 96,* 228 – 236, doi: 10.1785/0120050084.
872 Parsiegla, N., and U. Wegler (2008) Modelling of seismic energy transport at volcanoes with real
873 topography and complex propagation medium, *J. Volcanol. Geotherm. Res., 171,* 229–236, doi:
874 10.1016/j.jvolgeores.2007.12.001.
875 Petrosino, S., M. La Rocca and E. Del Pezzo (1999), Shallow velocity model of the northern flank of
876 Stromboli Volcano, deduced by high frequency surface wave dispersion, *J. Seismol., 3,* 83-94, doi:
877 10.1023/A:1009716203083.
878 Petrosino, S., P. Cusano, G. Saccorotti and E. Del Pezzo (2002), Seismic attenuation and shallow
879 velocity structures at Stromboli Volcano, Italy, *Bull. Seismol. Soc. Am., 92,* 1102-1116, doi:
880 10.1785/0120010147.
881 Petrosino, S., P. Cusano, and G. Saccorotti (2006), Shallow shear-wave velocity structure of Solfatara
882 volcano (Campi Flegrei, Italy), from inversion of Rayleigh-wave dispersion curves, *Boll. Geof.*
883 *Teo. Appli., 47,* 89-103.
884 Petrosino S., N. Damiano, P. Cusano, M. Veneruso, L. Zaccarelli, V. Torello, and E. Del Pezzo (2008),
885 Seismic noise at Solfatara Volcano (Campi Flegrei, Italy): acquisition techniques and first results,
886 *Quad. Geofis., 51,* 1-22, INGV, Italy.
887 Picozzi, M., S. Parolai, D. Bindi, and A. Strollo (2009): Characterization of shallow geology by high-
888 frequency seismic noise tomography, *Geophys. J. Int., 176,* 164-174, doi: 10.1111/j.1365-
889 246X.2008.03966.x.
890 Renalier, F., D. Jongmans, A. Savvaidis, M. Wathelet, B. Endrun, and C. Cornou (2010), Influence of
891 parameterization on inversion of surface wave dispersion curves and definition of an inversion
892 strategy for sites with a strong Vs contrast., *Geophysics, 75,* B197-B209, doi:10.1190/1.3506556.
893 Rigano, R., F. Cara, G. Lombardo, and A. Rovelli (2008), Evidence for ground motion polarization on

894 fault zones of Mount Etna volcano, *J. Geophys. Res.*, 113, B10306, doi:10.1029/2007JB005574.
895 Ritzwoller, M., and A. L. Levshin (1998), Eurasian surface wave tomography: group velocities, *J.*
896 *Geophys. Res., 103*, 4839–4878, doi: 10.1029/97JB02622.
897 Rosi, M., and A. Sbrana (1987), Phlegraean Fields, in *Quaderni de La Ricerca Scientifica*, 114, vol. 9,
898 edited by M. Rosi and A. Sbrana, pp. 175, CNR, Roma, Italy.
899 Rost, S., and C. Thomas (2002), Array seismology: methods and applications , *Reviews of Geophysics,*
900 *40*, 1008, 10.1029/2000RG000100.
901 Rovelli, A., A. Caserta, F. Marra, and V. Ruggiero (2002), Can seismic waves be trapped inside an
902 inactive fault zone? The case study of Nocera Umbra, central Italy, *Bull. Seismol. Soc. Am., 92*,
903 2217–2232, doi:10.1785/0120010288.
904 Saccorotti, G., R. Maresca and E. Del Pezzo (2001), Array analyses of seismic noise at Mt. Vesuvius
905 Volcano, *J. Volcanol. Geotherm. Res.,110*, 79-106, doi:10.1016/S0377-0273(01)00204-9.
906 Saccorotti G., B. Chouet, and P. Dawson, (2003), Shallow-velocity models at the Kilauea Volcano,
907 Hawaii, determined from array analyses of tremor wavefields, *Geophys. J. Int., 152*, 633-648,
908 doi:10.1046/j.1365-246X.2003.01867.x.
909 Saccorotti, G., S. Petrosino, F. Bianco, M. Castellano, D. Galluzzo, M. La Rocca, E. Del Pezzo, L.
910 Zaccarelli, and P. Cusano (2007), Seismicity associated with the 2004–2006 renewed ground uplift
911 at Campi Flegrei Caldera, Italy, *Phys. Earth Planet. Inter. 165*, 14–24,
912 doi:10.1016/j.pepi.2007.07.006.
913 Salvini, F., A. Billi, and D.U. Wise (1999), Strike-slip fault-propagation cleavage in carbonate rocks:
914 the Mattinata fault zone, Southern Apennines, Italy, *J. Struct. Geol., 21*, 1731-1749,
915 doi:10.1016/S0191-8141(99)00120-0.
916 Sambridge, M. (1999), Geophysical inversion with a neighborhood algorithm: I. Searching a parameter
917 space, *Geophys. J. Int., 138*, 479-494, doi:10.1046/j.1365-246x.1999.00900.x.

Stehly, L., B. Fry, M. Campillo, N. M. Shapiro, J. Guilbert, L. Boschi and D. Giardini (2009), Tomography of the Alpine region from observations of seismic ambient noise, *Geophys. J. Int*, *178*, 338–350, doi:10.1111/j.1365-246X.2009.04132.x.

Tonarini, S., M. D'Antonio, M. A. Di Vito, G. Orsi, and A. Carandente (2009), Geochemical and B-Sr-Nd isotopic evidence for mingling and mixing processes in the magmatic system that fed the Astroni volcano (4.1-3.8 ka) within the Campi Flegrei caldera (Southern Italy), *Lithos, 107,* 135-151, doi:10.1016/j.lithos.2008.09.012.

Vilardo, G., R. Isaia, G. Ventura, P. De Martino, and C. Terranova (2010), InSAR Permanent Scatterer analysis reveals fault re-activation during inflation and deflation episodes at Campi Flegrei caldera, *Rem. Sens. Env., 114*, 2373–2383, doi:10.1016/j.rse.2010.05.014.

Wathelet, M., D. Jongmans, and M. Ohrnberger (2004), Surface wave inversion using a direct search algorithm and its application to ambient vibration measurements, *Near Surf. Geophys., 2*, 211—221.

Wathelet, M., D. Jongmans, and M. Ohrnberger (2005), Direct inversion of spatial autocorrelation curves with the neighborhood algorithm, *Bull. Seismol. Soc. Am., 95*, 1787—1800, doi:10.1785/0120040220.

Wathelet, M., D. Jongmans, M. Ohrnberger, and S. Bonnefoy-Claudet (2008), Array performances for ambient vibrations on a shallow structure and consequences over Vs inversion, *J. Seismol., 12*, 1-19, doi:10.1007/s10950-007-9067-x.

Wegler, U., and B. G. Luhr (2001), Scattering behaviour at Merapi volcano (Java) revealed from an active seismic experiment, *Geophys. J. Int., 145*, 579–592, doi:10.1046/j.1365-246x.2001.01390.x.

Wegler, U. (2003), Analysis of multiple scattering at Vesuvius volcano, Italy, using data of the TomoVes active seismic experiment, *J. Volc. Geotherm. Res., 128*, 45–63, doi:10.1016/S0377-0273(03)00246-4.

Yang, J., and T. Sato (2000), Interpretation of seismic vertical amplification observed at an array site *Bull. Seismol. Soc. Am., 90*, 275-285, doi:10.1785/0119990068.

Yang, J. (2006), Frequency-dependent amplification of unsaturated surface soil layer, *J. Geotech. Geoenv. Eng., 132*, 526-531, doi: 0.1061/(ASCE)1090-0241(2006)132:9(1229).

Zollo, A., N. Maercklin, M. Vassallo, D. Dello Iacono, J. Virieux, and P. Gasparini (2008), Seismic reflections reveal a massive melt layer feeding Campi Flegrei caldera, *Geophys. Res. Lett., 35*, L12306, doi:10.1029/2008GL034242.

966 **Figure captions**

967 Fig. 1 a) Structural sketch map of the Solfatara volcano and surroundings, with seismic array geometry,
968 vents and structural analysis site locations, and W-E cross-section profile; b) detail of the array
969 geometry, and location of SFT seismic station; c) location of the study area in the Campi Flegrei
970 caldera (after *Orsi et al.* [1996]).

971

972 Fig. 2 Contoured stereo-net pole-frequency (Schmidt projections, lower hemisphere) and normalized
973 azimuth-frequency (rose) diagrams of the meso-structural data sampled in (a) sites 1, 2, 3 and 4 and (b)
974 sites 5, 6 and 7 at the Solfatara volcano and surroundings (using DAISY software by *Salvini et al.*
975 [1999]). See the text for a discussion of the detected fracture attitudes.

976

977 Fig. 3 RMS of the seismic noise recorded at SFT station (vertical component) in the period 2-8 April
978 2007. Data were filtered in the 1-20 Hz frequency band. Each point is the average over 1-hour long
979 time window.

980

981 Fig. 4 168 H/V spectral ratios calculated for 1-hour recordings of seismic noise at SFT station over the
982 whole period 2-8 April 2007.

983

984 Fig. 5 Maps of the resonance frequency (left) and peak amplitude (right) calculated from the
985 application of Nakamura's technique [*Nakamura*, 1989] to ambient noise recorded at the Solfatara
986 volcano. The limits of the plots correspond to the white box drawn in Figure 1; the geographical
987 coordinates are expressed in meters in the UTM system. Black triangles indicate the array seismic
988 stations.

989

990 Fig. 6 Phase velocity dispersion curves for the 5 arrays obtained from the application of the f-k method.

991

992 Fig. 7 Phase velocity dispersion curves for the 5 arrays obtained from the application of the modified
993 SPAC technique.

994

995 Fig. 8 Statistical analysis to test the parameterization influence on the inversion procedure: minimum
996 misfit versus number of layers over half space (on left) and half space depth (on the right). A common
997 legend at left-bottom illustrates the correspondence between the symbols and the arrays.

998

999 Fig. 9 Inversion results the arrays A, B, C, D and E. Left: theoretical dispersion curves of Rayleigh
1000 waves calculated from the inversion procedure. Color tonality is proportional to the misfit according to
1001 the common palette showed at the bottom of the figure and black lines represent the experimental
1002 curves with the error bars. Centre: 1-D S-wave velocity profiles obtained from the inversion of the
1003 experimental dispersion curves; black lines indicate the mean model (continuous) and the standard
1004 deviation (dashed) calculated from Monte Carlo algorithm. The profiles for arrays C and E are
1005 represented down to a depth of 40 m according to the corresponding resolution depth. Right: theoretical
1006 ellipticity curves of Rayleigh waves computed for all the velocity models. The grey vertical bars
1007 highlight the experimental H/V peaks and the corresponding error used to constrain the inversions.

1008

1009 Fig. 10 3-D S-wave velocity model for the Solfatara volcano. Horizontal slices show the S-wave
1010 velocity isolines (labels in m/s) at the depth indicated in the upper left corner. The S-wave velocity
1011 values are represented according to the color bar at the bottom of the figure. The limits of the plots
1012 correspond to the white box drawn in Figure 1; geographical coordinates are expressed in meters in the
1013 UTM system. Black triangles and white labels indicate the array seismic stations. The velocity values

for arrays C and D do not appear in the panel h and i since these arrays have no resolution below 40 m. The arrays A, B and D resolve to a maximum depth of 200 m.

Fig. 11 Rose diagrams of the azimuth of horizontal polarization of ambient noise. Stations for which the percentage of rectilinearity (RL) is equal or greater is at least 70% are represented. The blue arrows indicate the vector field interpolated from a gridding procedure. The limits of the plot correspond to the white box drawn in Figure 1; geographical coordinates are expressed in meters in the UTM system.

Fig. 12 Interpretative W-E geological cross-section of the Solfatara volcano (see text for explanation). At the bottom, the corresponding S-wave velocity model from arrays E, A and D, represented along the same W-E profile is shown.

Top	Lithostratigraphic Unit	Lithology	Section 1	Section 3	Section 4	Section 6
Solfatara Tephra	Tephra of vent 2	Fine-ash surge beds with minor pumice fallout layers and lenses, and lithic blocks. The beds are undulated to plane-parallel. This deposit is coarser and thicker in the eastern and northern parts of the crater. It thins radially from vent 2 and drapes unconformably parts of the inner walls of crater 1.	Thickness = 0-13 m. The thickness variation is due to pinch-out of the surge sequence against the inner walls of crater 1.	Thickness = 2-14 m. The thickness variation is due to pinch-out of the surge sequence against the inner walls of crater 1 and to partial draping of crater 1 rim.	Thickness = 3 m.	Thickness = 1.7 m.
	Angular unconformity 2					
	Tephra of vent 1	Coarse- to fine-ash surge beds and minor scattered or aligned coarse pumice fragments and lithic blocks. The beds are massive to plane parallel, and yellowish to green in color. They contain abundant accretionary lapilli. This deposit is exposed along all the inner crater slopes.	Thickness ≥ 15 m, base not exposed.	Thickness = 7 m.	Thickness = 6 m.	Thickness = 3.9 m.
	Angular unconformity 1					
Bottom	Basal Breccia	Very coarse breccia deposit with a fine grained ash matrix. It is composed by variably altered lithic fragments (tuff and lava) and scoria bombs. It is exposed along the eastern inner crater walls.	Not exposed	Thickness = 8 m.	Thickness = ca. 2 m.	Thickness ≥ 4 m, base not exposed.

Table 1

Description of the main lithological and stratigraphical characteristics of the Solfatara Tephra, from base upwards. See the text for discussion. Sections numbers are the same of the structural analysis, reported in Figure 1.

Array Radius (m)	kmin/2 (rad/m)	kmax (rad/m)
5	0.257	0.648
10	0.138	0.38
25	0.055	0.157
50	0.024	0.112
100	0.013	0.057

Table 2

Values of minimum (kmin/2) and maximum (kmax) resolvable wavelength for the different array configurations.

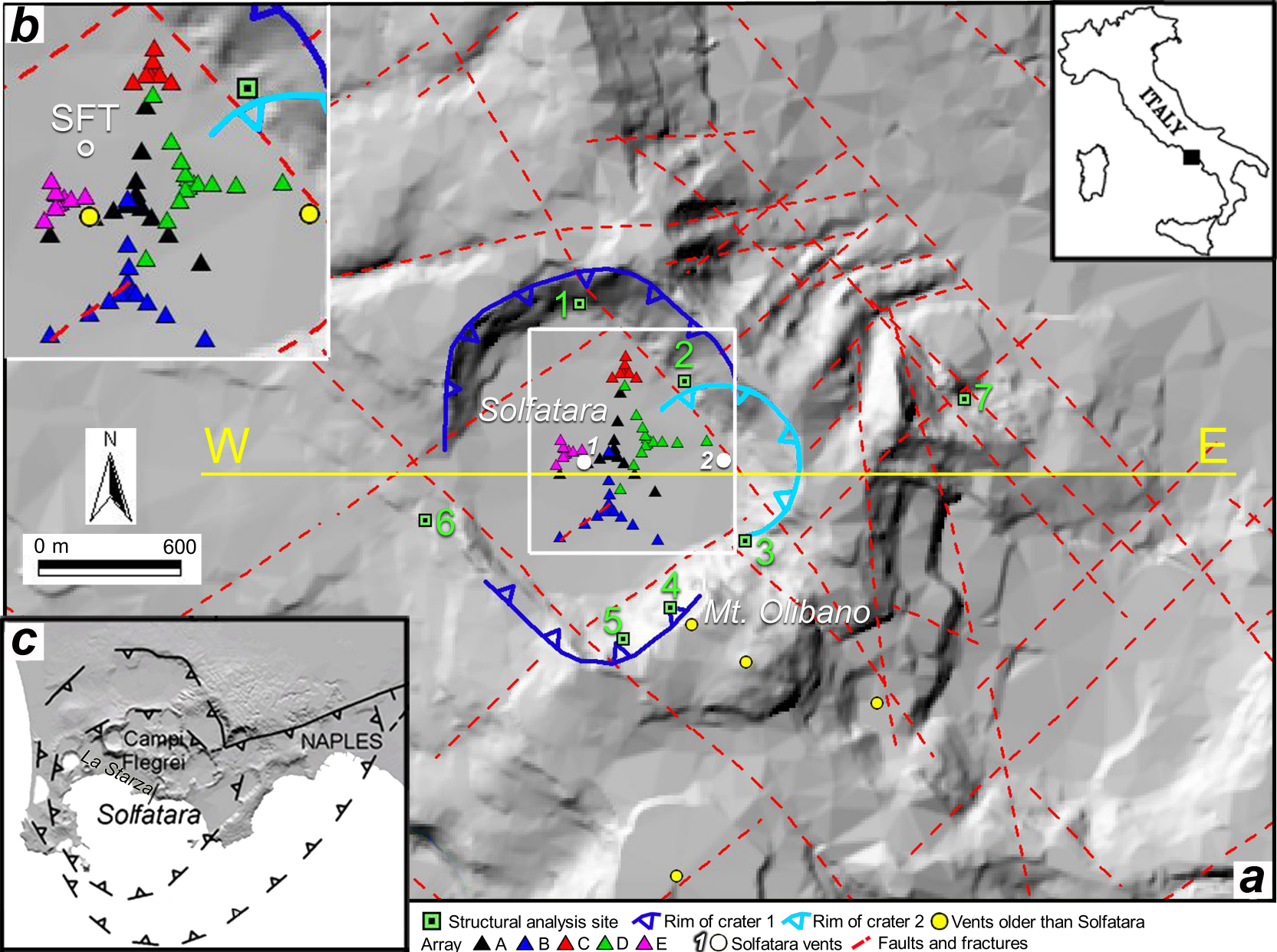
b
SFT
ITALY
1
2
Solfatara
1
2
7
W
E
N
0 m
600
6
3
4
5
Mt. Olibano
c
Campi Flegrei
NAPLES
La Starza
Solfatara
a
Structural analysis site
Rim of crater 1
Rim of crater 2
Vents older than Solfatara
Array A B C D E
Solfatara vents
Faults and fractures

SFT - 1

Frequency Gaussians
Total Data: 71 max: 11 min: 0 mean: 100,313 sd: 4,888 mode: 90

RMS = 0,1058319

GAUSSIAN PARAMETERS					
#	%	Nor. H.	Max H.	Azimuth	sd
1	18,41	100,00	1,994	-90,97°	4,36°
2	18,51	69,14	1,379	-65,96°	6,34°
3	20,32	46,12	0,9199	34,64°	10,42°
4	6,789	48,54	0,9680	-0,9378°	3,31°
5	24,19	56,37	1,124	-24,36°	10,16°
6	12,78	39,68	0,7914	67,85°	7,62°

Base Fit Value = 0,001

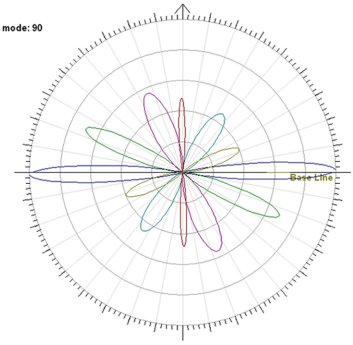

Data Number: 71

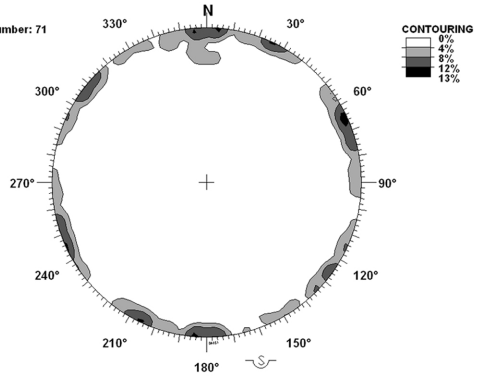

SFT - 2

Frequency Gaussians
Total Data: 68 max: 16 min: 0 mean: 133,843 sd: 4,793 mode: -60

RMS = 0,1977608

GAUSSIAN PARAMETERS					
#	%	Nor. H.	Max H.	Azimuth	sd
1	45,87	100,00	2,875	-64,22°	7,21°
2	30,56	74,73	2,149	26,67°	6,43°
3	16,78	20,32	0,5842	-9,923°	12,99°

Base Fit Value = 0,001

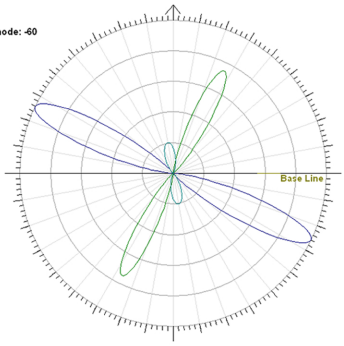

Data Number: 68

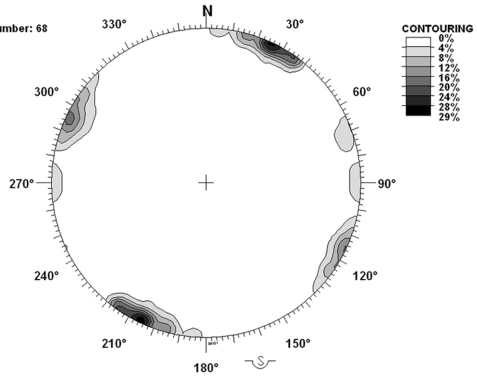

SFT - 3

Frequency Gaussians
Total Data: 45 max: 7 min: 0 mean: -40,497 sd: 5,159 mode: 90

RMS = 7,928252E-02

GAUSSIAN PARAMETERS					
#	%	Nor. H.	Max H.	Azimuth	sd
1	19,69	100,00	1,257	-90,95°	4,69°
2	20,69	86,91	1,092	-3,525°	5,67°
3	17,67	85,90	1,079	-62,67°	4,9°
4	15,18	72,72	0,9138	-38,97°	4,97°
5	21,45	56,61	0,7114	40,04°	9,02°
6	5,315	38,90	0,4888	19,44°	3,27°

Base Fit Value = 0,001

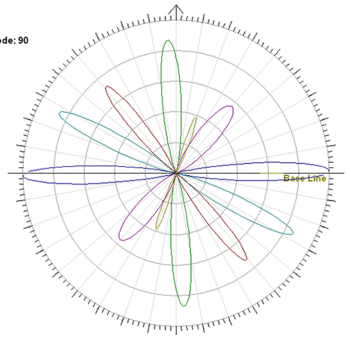

Data Number: 45

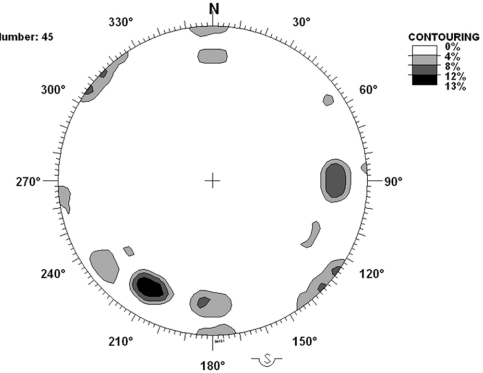

SFT - 4

Frequency Gaussians
Total Data: 20 max: 9 min: 0 mean: 55,722 sd: 4,004 mode: 50

RMS = 3,749029E-02

GAUSSIAN PARAMETERS					
#	%	Nor. H.	Max H.	Azimuth	sd
1	46,37	100,00	1,684	49,00°	3,67°
2	30,91	66,67	1,123	-21,00°	3,67°
3	25,76	55,56	0,9355	89,00°	3,67°

Base Fit Value = 0,001

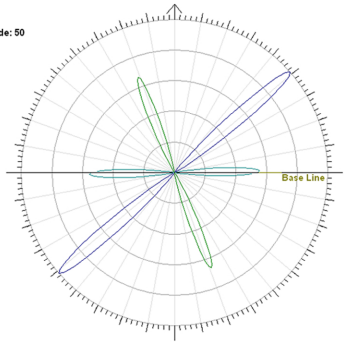

Data Number: 20

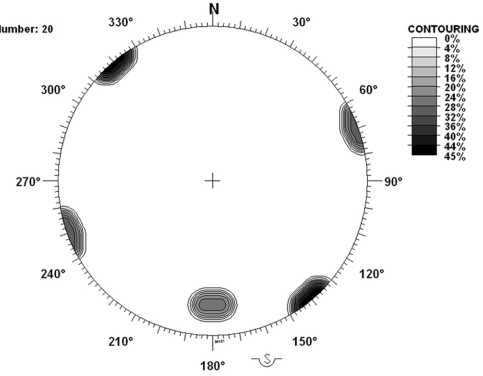

SFT - 5 lava

Frequency Gaussians
Total Data: 29 max: 8 min: 0 mean: 74,979 sd: 2,910 mode: 90

RMS = 8,701871E-02

GAUSSIAN PARAMETERS					
#	%	Nor. H.	Max H.	Azimuth	sd
1	33,79	100,00	1,413	87,87°	4,61°
2	50,55	50,96	0,7202	52,36°	13,53°
3	16,04	34,16	0,4828	-43,60°	6,4°

Base Fit Value = 0,001

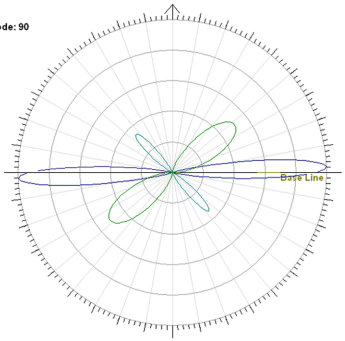

Data Number: 29

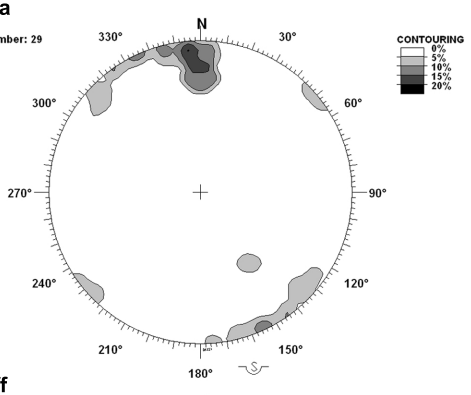

SFT - 5 tuff

Frequency Gaussians
Total Data: 17 max: 9 min: 0 mean: 75,829 sd: 3,432 mode: 70

RMS = 3,344366E-02

GAUSSIAN PARAMETERS					
#	%	Nor. H.	Max H.	Azimuth	sd
1	54,55	100,00	1,684	69,00°	3,67°
2	24,24	44,44	0,7484	-1,0000°	3,67°
3	24,24	44,44	0,7484	-71,00°	3,67°

Base Fit Value = 0,001

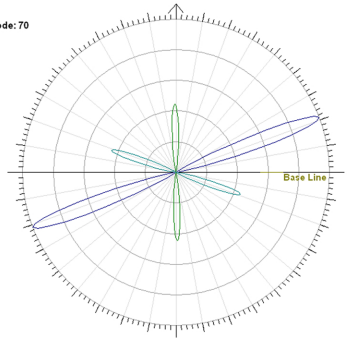

Data Number: 17

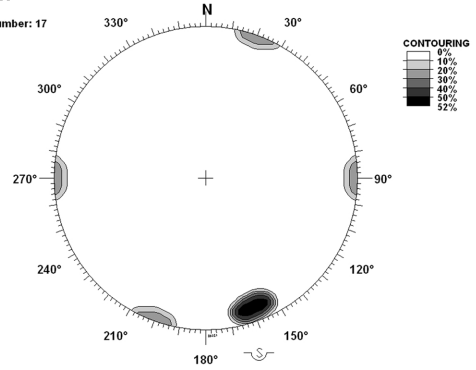

SFT - 6

Frequency Gaussians
Total Data: 37 max: 9 min: 0 mean: 56,345 sd: 4,996 mode: 60

RMS = 7,314986E-02

GAUSSIAN PARAMETERS					
#	%	Nor. H.	Max H.	Azimuth	sd
1	26,40	100,00	1,681	58,76°	3,87°
2	22,17	89,22	1,500	-40,98°	3,64°
3	20,64	78,19	1,315	39,29°	3,87°
4	13,92	55,64	0,9355	-1,0000°	3,67°
5	13,77	55,87	0,9394	-61,07°	3,61°

Base Fit Value = 0,001

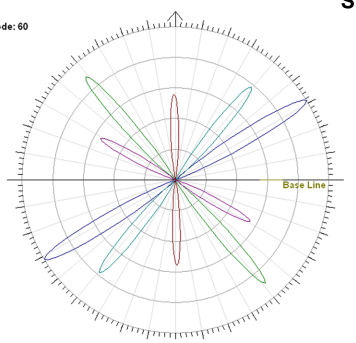

Data Number: 37

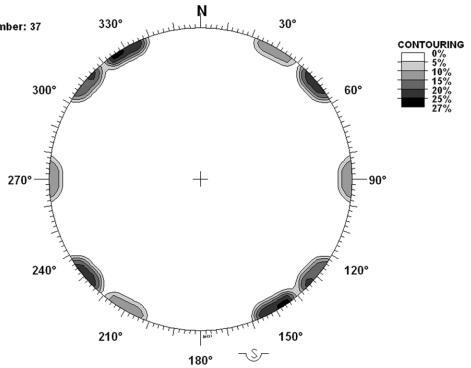

SFT - 7

Frequency Gaussians
Total Data: 43 max: 7 min: 0 mean: 8.140 sd: 61.499 mode: -70

GAUSSIAN PARAMETERS					
#	%	Nor. H.	Max H.	Azimuth	sd
1	18.7	100.0	1.23	-70.8°	4.4°
2	16.7	90.4	1.11	29.1°	4.3°
3	16.0	87.8	1.08	88.8°	4.2°
4	12.6	61.5	0.75	-59.8°	4.8°
5	10.0	42.2	0.52	-32.5°	5.5°
6	10.0	40.6	0.50	75.3°	5.7°
7	5.5	36.0	0.44	39.6°	3.6°
8	5.8	36.3	0.45	18.5°	3.7°
9	5.3	30.0	0.37	60.0°	4.2°

Min Value Fit = 0.001

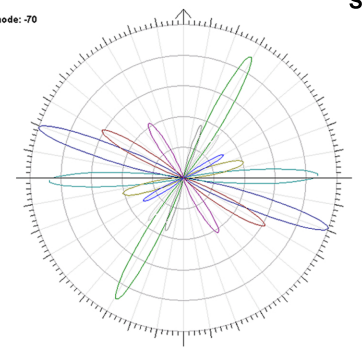

Data Number: 43

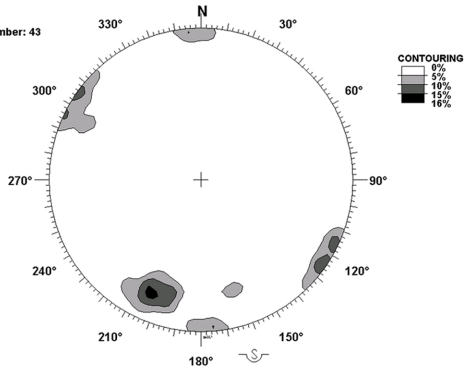

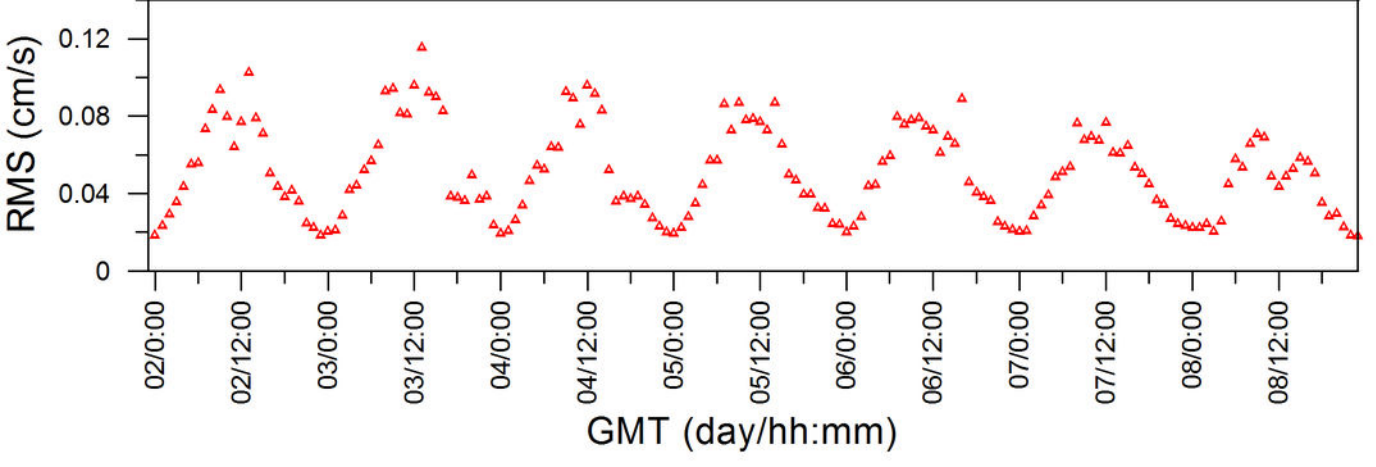
RMS (cm/s)
0.12
0.08
0.04
0
02/0:00
02/12:00
03/0:00
03/12:00
04/0:00
04/12:00
05/0:00
05/12:00
06/0:00
06/12:00
07/0:00
07/12:00
08/0:00
08/12:00
GMT (day/hh:mm)

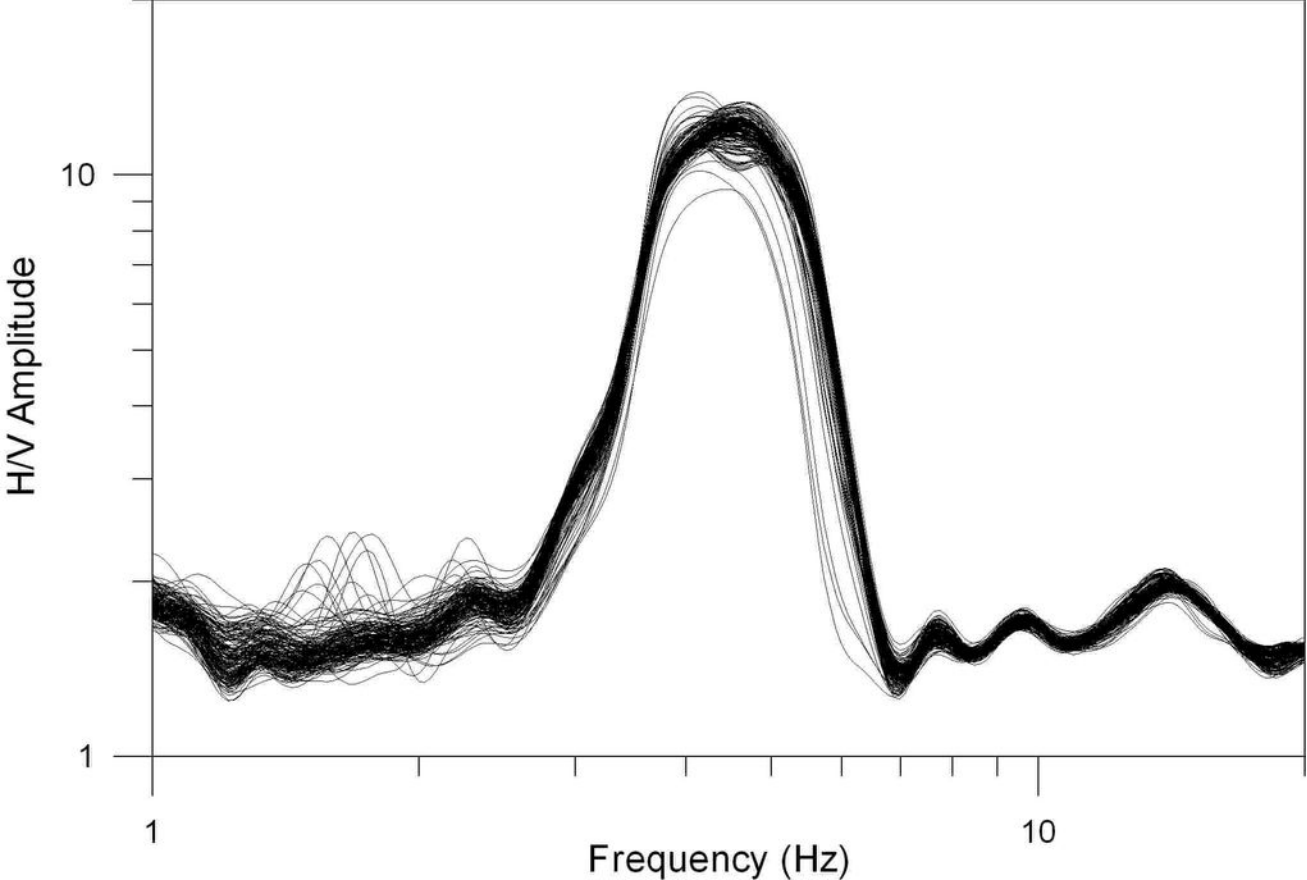
10
1
H/V Amplitude
1
10
Frequency (Hz)

Resonance Frequency

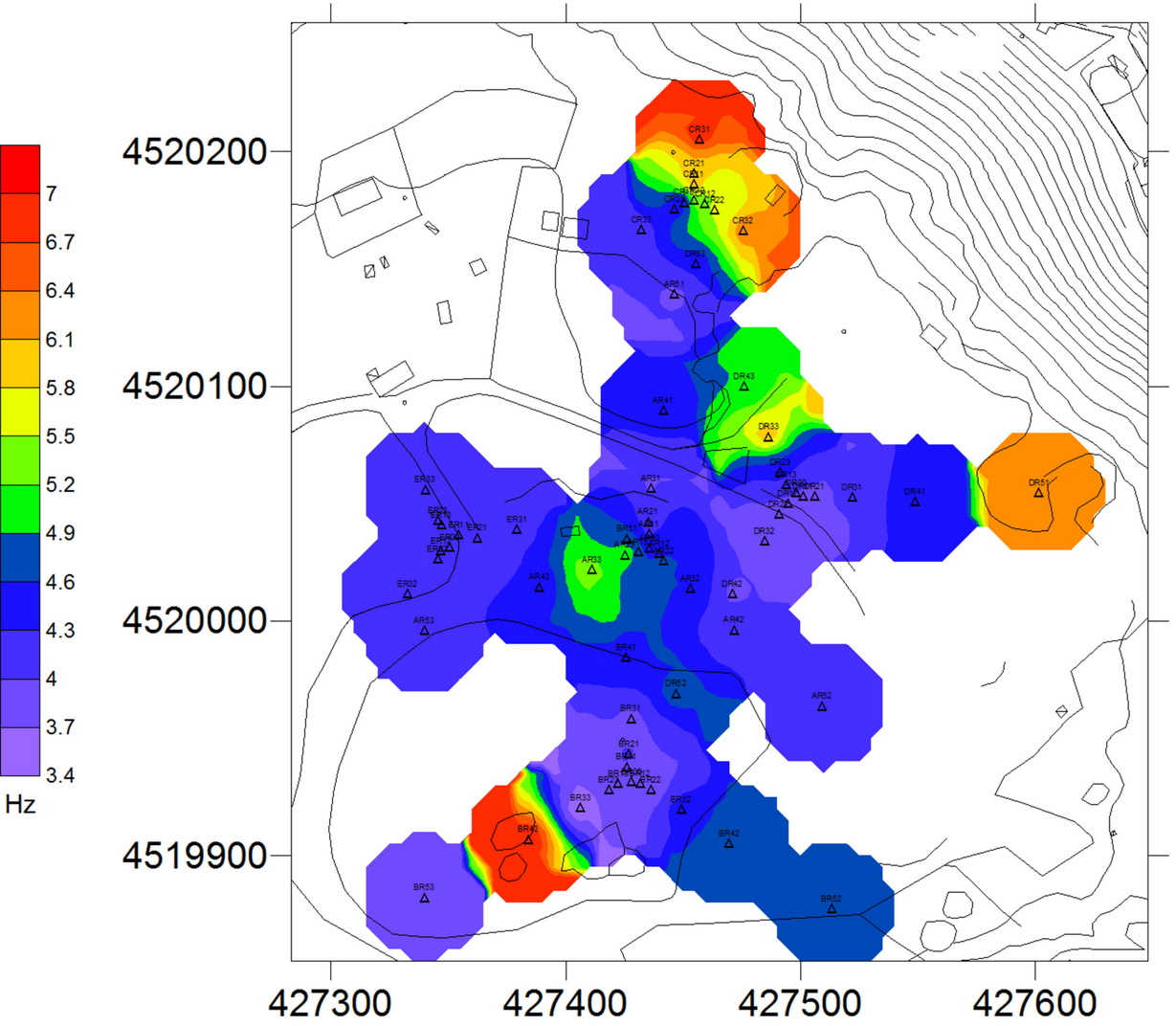

Peak Amplitude

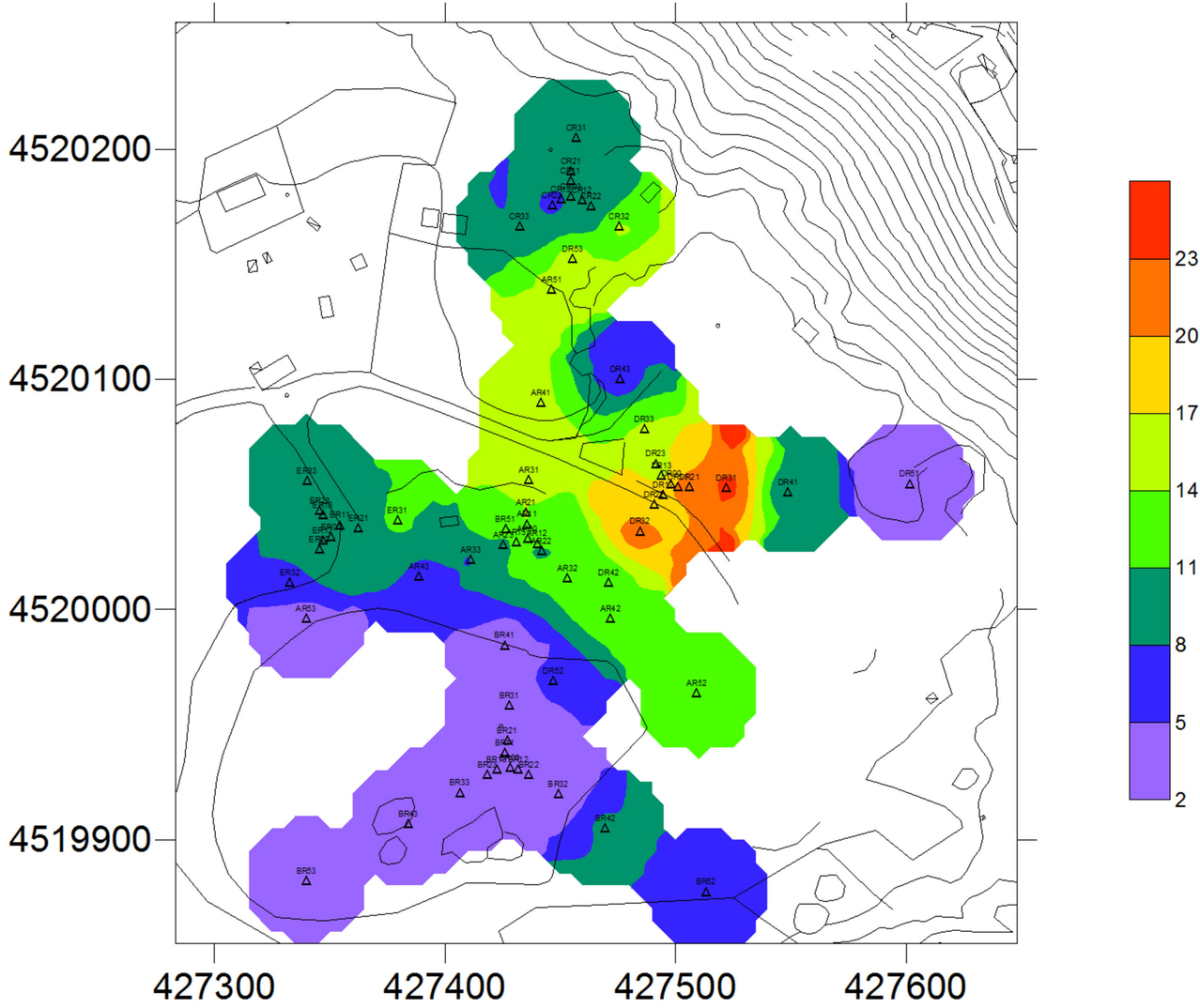

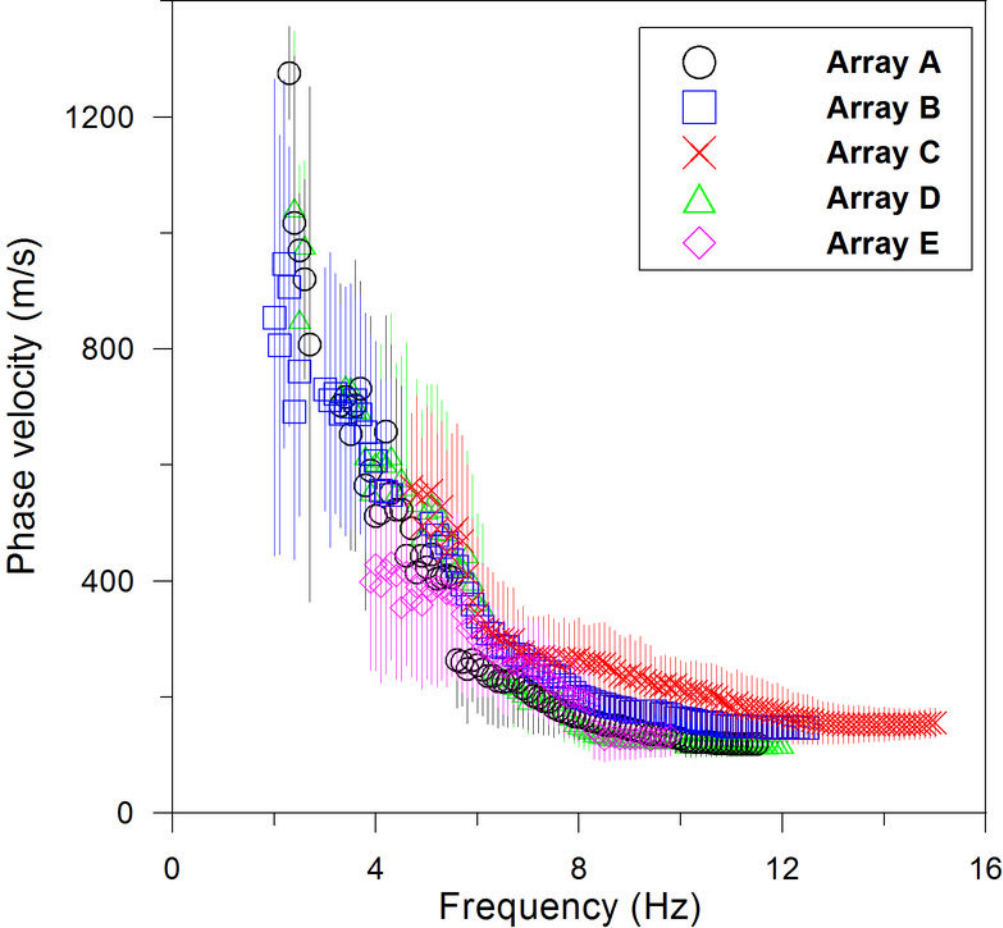
Array A
Array B
Array C
Array D
Array E
Phase velocity (m/s)
1200
800
400
0
0
4
8
12
16
Frequency (Hz)

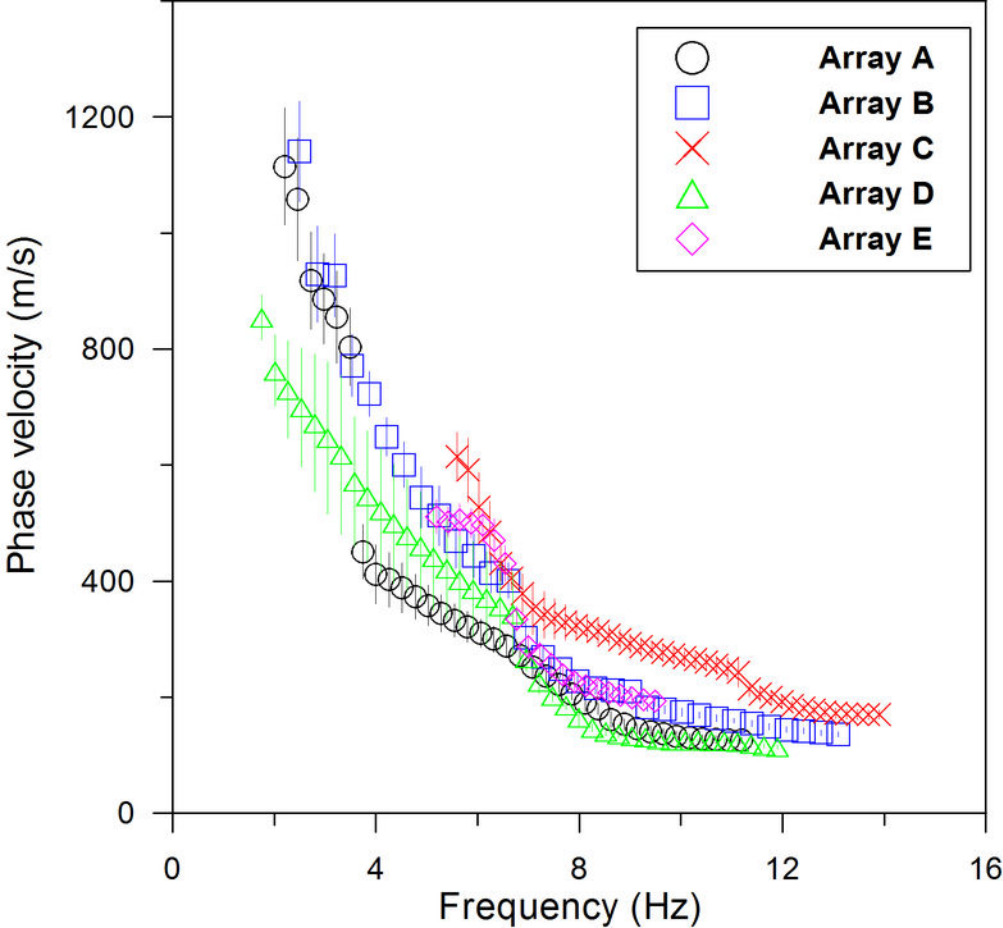
Array A
Array B
Array C
Array D
Array E
Phase velocity (m/s)
1200
800
400
0
0
4
8
12
16
Frequency (Hz)

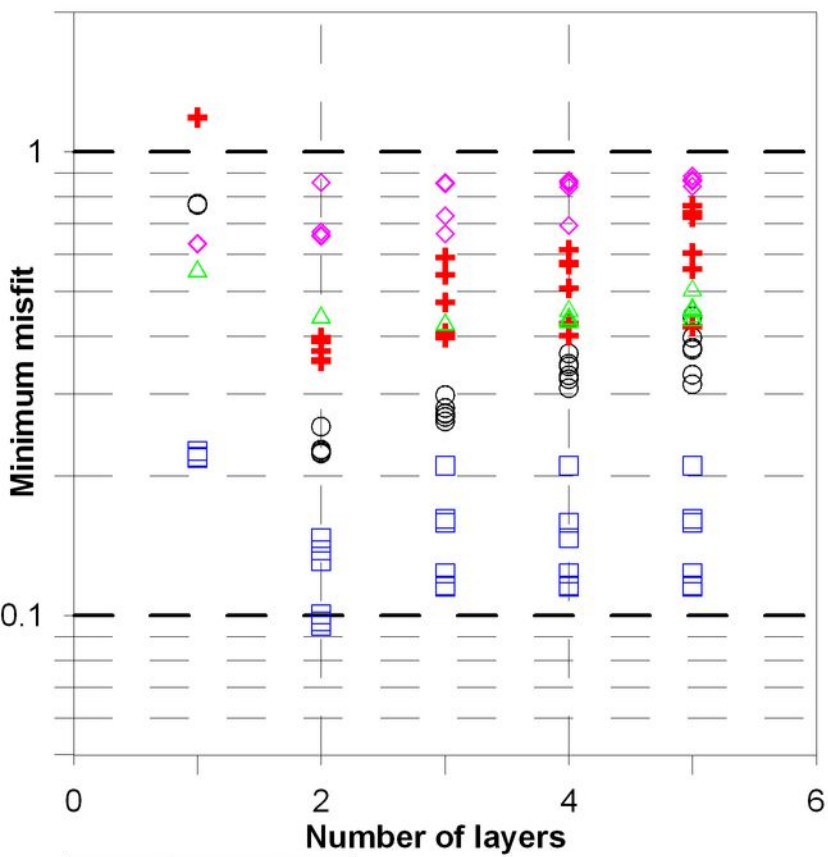
Minimum misfit
1
0.1
0
2
4
6
Number of layers

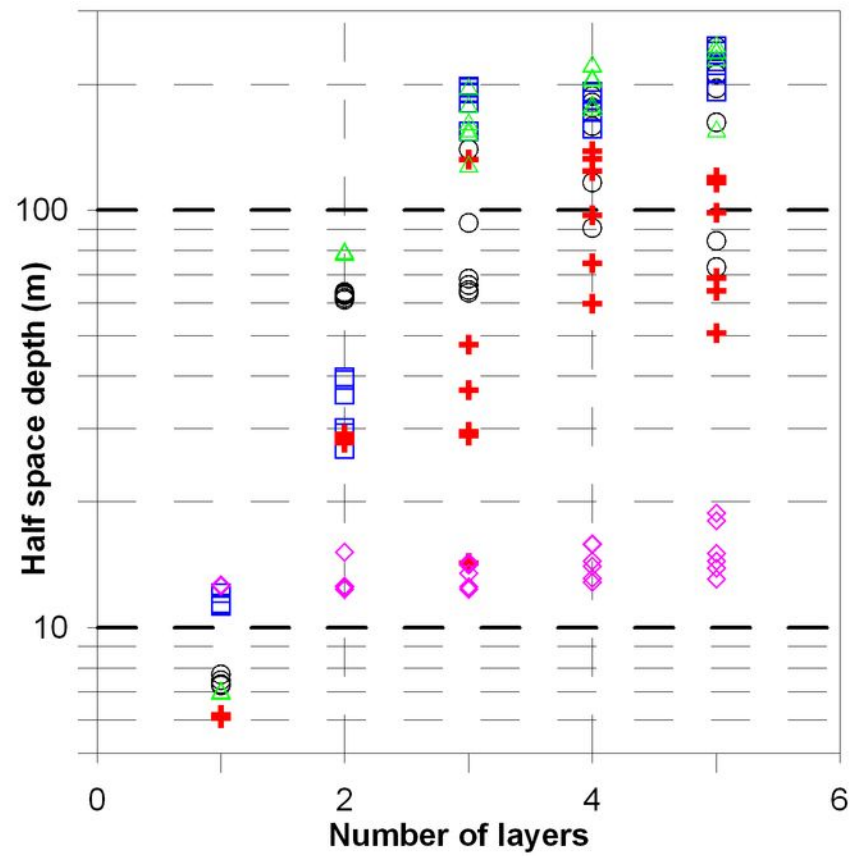
Half space depth (m)
100
10
0
2
4
6
Number of layers


Array A
Array B
Array C
Array D
Array E

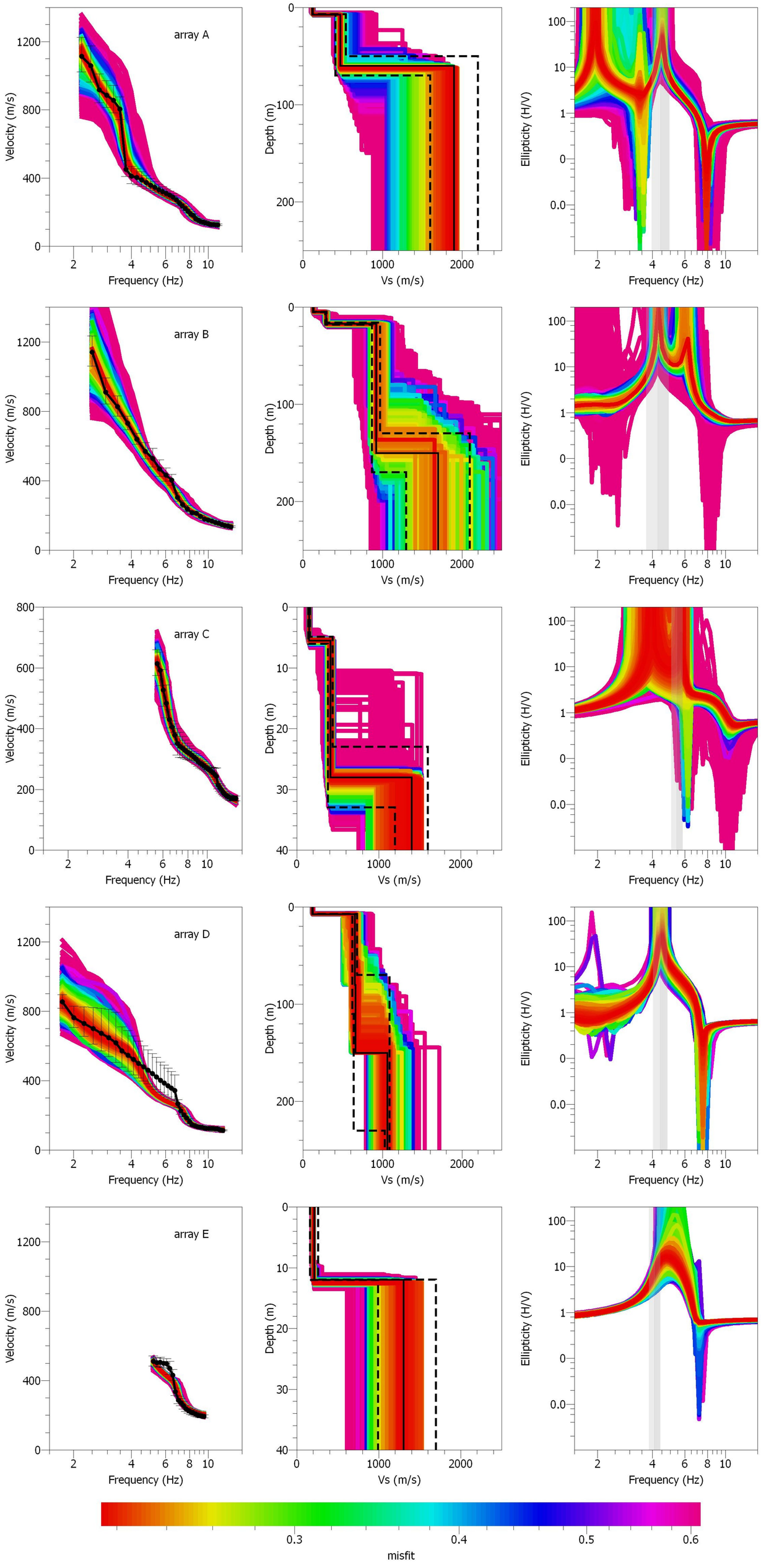
array A
array B
array C
array D
array E
Velocity (m/s)
Frequency (Hz)
Depth (m)
Vs (m/s)
Ellipticity (H/V)
misfit
0.3
0.4
0.5
0.6

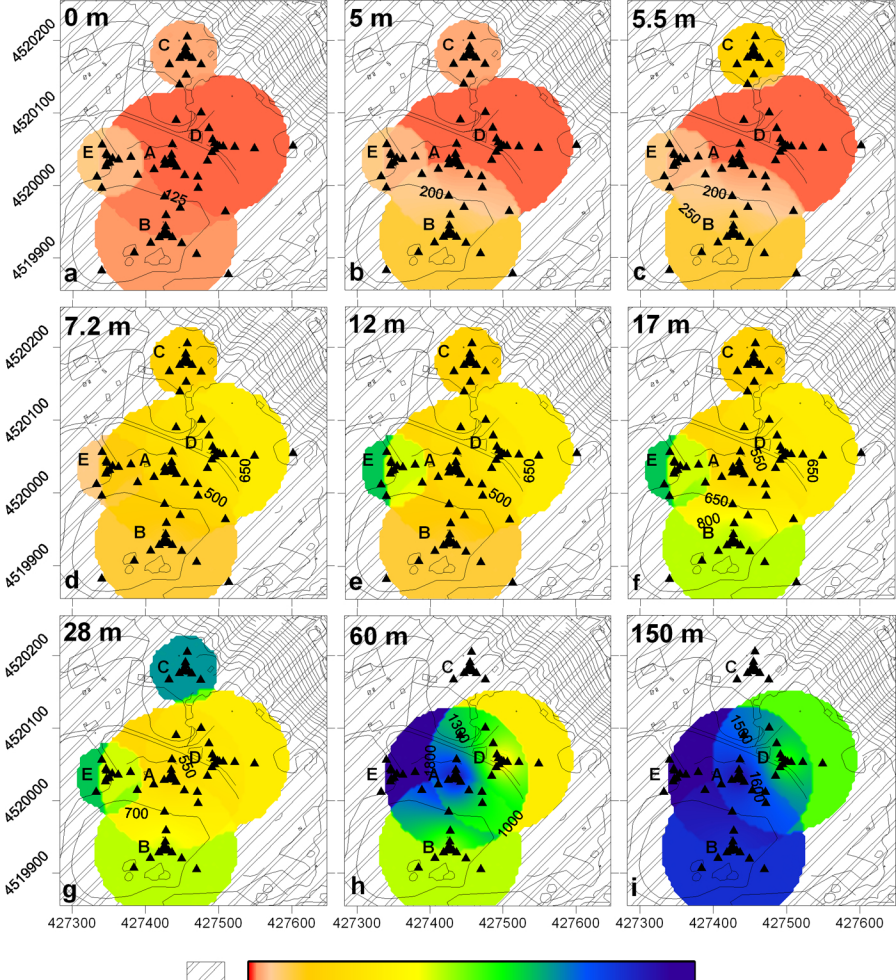
0 m
5 m
5.5 m
7.2 m
12 m
17 m
28 m
60 m
150 m
a
b
c
d
e
f
g
h
i
A
B
C
D
E
425
200
250
500
650
700
1000
1600
4520200
4520100
4520000
4519900
427300
427400
427500
427600
No Data
100 300 500 700 900 1100 1300 1500 1700 1900
S-wave velocity (m/s)

4520200
4520100
4520000
4519900
427300
427400
427500
427600
CR31
CR21
CR11
CR12
CR33
CR32
DR53
AR31
DR43
DR33
DR23
DR13
DR21
DR31
DR41
DR51
DR32
ER23
ER11
ER31
ER32
BR00
BR33
BR52

W
(UTM coord 426720, 4520000)

100 m a.s.l.

s.l.

Crater 1

Crater 2

E
(UTM coord 428534, 4520000)

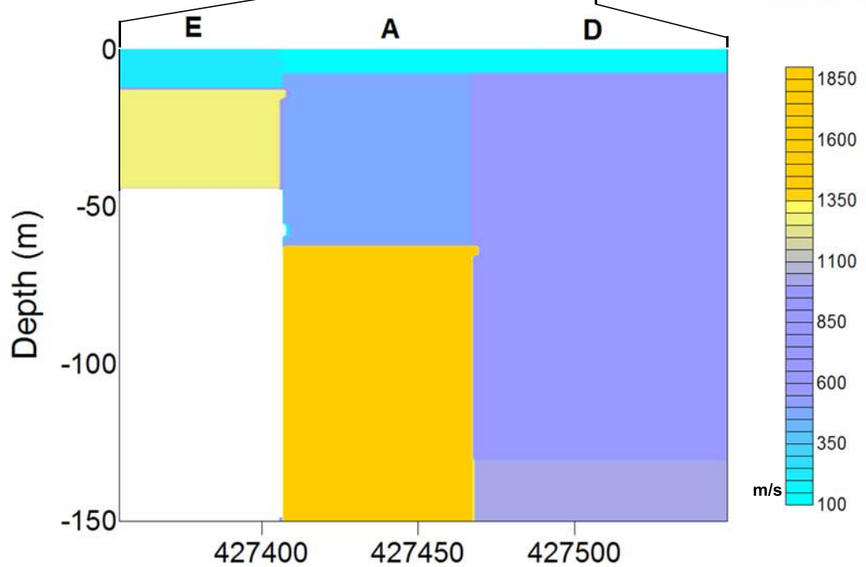

- Reworked deposits
- Astroni Tephra
- Tephra of vent 2
- Lava domes
- Tephra of vent 1

Solfatara deposits

- Agnano 3 - Agnano Monte Spina complex
- La Starza marine and transitional deposits
- Faults and fractures